# Simultaneous regulation of cytokinetic furrow and nucleus positions by cortical tension contributes to proper DNA segregation during late mitosis

Anne Pacquelet, Matthieu Jousseaume, Jocelyn Etienne, Grégoire Michaux

## To cite this version:

Anne Pacquelet, Matthieu Jousseaume, Jocelyn Etienne, Grégoire Michaux. Simultaneous regulation of cytokinetic furrow and nucleus positions by cortical tension contributes to proper DNA segregation during late mitosis. Current Biology - CB, 2019, 29 (22), pp.3766-3777.e4. 10.1016/j.cub.2019.09.013. hal-02351117

HAL Id: hal-02351117
https://hal.science/hal-02351117v1

Submitted on 6 Nov 2019

# Simultaneous regulation of cytokinetic furrow and nucleus positions by cortical tension contributes to proper DNA segregation during late mitosis

**Authors:**

Anne Pacquelet[1,*], Matthieu Jousseaume[1], Jocelyn Etienne[2], Grégoire Michaux[1]

[*] Corresponding author

**Affiliations :**

[1] Univ Rennes, CNRS, IGDR (Institut de Génétique et de Développement de Rennes), UMR 6290, 2 avenue du Professeur Léon Bernard, 35000 Rennes, France

[2] Univ Grenoble Alpes, CNRS, LIPhy, 140 Avenue de la Physique, 38402 Saint Martin d'Hères, France

**Contact information:**

anne.pacquelet@univ-rennes1.fr

CNRS UMR6290 - IGDR

2 avenue du Professeur Léon Bernard

35043 Rennes Cedex

France

Tel: + (33) 2 2323 5598

Fax: + (33) 2 2323 4478

**Lead contact:** Anne Pacquelet, anne.pacquelet@univ-rennes1.fr

**Running title: Regulation of furrow and nuclear position by cortical tension**

## Summary

Coordinating mitotic spindle and cytokinetic furrow positioning is essential to ensure proper DNA segregation. Here we present a novel mechanism, which corrects DNA segregation defects due to cytokinetic furrow mispositioning during the first division of *C. elegans* embryos. Correction of DNA segregation defects due to an abnormally anterior cytokinetic furrow relies on the concomitant and opposite displacements of the furrow and of the anterior nucleus, towards the posterior and anterior poles of the embryo, respectively. It also coincides with cortical blebbing and an anteriorly directed cytoplasmic flow. While microtubules contribute to nuclear displacement, relaxation of an excessive tension at the anterior cortex plays a central role in the correction process and simultaneously regulates cytoplasmic flow as well as nuclear and furrow displacements. This work thus reveals the existence of a so far uncharacterized correction mechanism, which is critical to correct DNA segregation defects due to cytokinetic furrow mispositioning.

## Introduction

Ensuring equal DNA segregation is a critical feature of cell division. The correct assembly of the mitotic spindle at metaphase followed by the separation of sister chromatids at anaphase are essential steps in this process. Ingression of the cytokinetic furrow between the separated chromatids then ensures that the genetic material is equally inherited by the two daughter cells. It is therefore crucial that the positions of the cytokinetic furrow and the mitotic spindle are well coordinated. Two main signalling pathways emanating from the mitotic spindle control furrow position by restricting the localization of myosin contractile ring components to the vicinity of the central spindle [1,2]. First, the centralspindlin complex, which localizes both at the central spindle and at the adjacent equatorial cortex, activates myosin contractility through the regulation of the small GTPase Rho [3–5]. Second, astral microtubules prevent myosin activity at the pole of dividing cells, through mechanisms that remain to be precisely determined [6–10]. However, asymmetrically localized myosin also contributes to furrow localization [11–13]. During the first division of the one-cell *C. elegans* embryo, myosin transiently accumulates at the anterior cortex at early anaphase before being restricted to the equatorial cortex, at the presumptive furrow ingression site [13]. This dynamic localization of myosin is tightly regulated. In particular, in embryos lacking both the kinase PIG-1 and the anillin ANI-1, myosin abnormally accumulates at the anterior cortex and leads to the displacement of the cytokinetic furrow, which position is thus no longer coordinated with the position of the mitotic spindle [13].

Mistakes occurring at any of the successive steps of mitosis may impair DNA segregation. However, several mechanisms, such as the spindle assembly [14] or the abscission checkpoints [15,16], limit the occurrence of detrimental DNA segregation defects. In this study, we identify and characterize a new type of correction mechanism, which prevents DNA segregation defects resulting from the lack of coordination between cytokinetic furrow and mitotic spindle positions.

## Results

### DNA segregation defects due to furrow mispositioning can be corrected

In *ani-1(RNAi);pig-1(gm344)* embryos (further referred to as *ani-1;pig-1*), excessive myosin accumulation at the anterior cortex displaces the furrow towards the anterior of the embryo. As a result, the two nuclei are often both located on the posterior side of the furrow (17/20 embryos, Figure 1A, t=300 or 380 sec, Video S1) [13]. However, most of those DNA segregation defects are corrected, with the anterior nucleus finally being located on the anterior side of the furrow (16/17 embryos, Figure 1A, t=540 sec, Video S1). After correction, furrow ingression completes in 13/16 embryos and persists until the beginning of the second division in 8/16 embryos. Moreover, the anterior nucleus contained the expected number (i.e. 12) of chromosomes (n=10 embryos, Video S2). Hence, the correction process ensures that each daughter cell inherits the correct number of chromosomes.

As cytokinesis is delayed in *ani-1;pig-1* embryos (e.g. Figure 1A), we asked when the correction of DNA segregation defects occurs relative to other cell cycle events. We first monitored nuclear envelope reformation. Both in control and *ani-1;pig-1* embryos, nuclear envelope reassembles during cytokinesis (Figure 1B, Video S3). In *ani-1;pig-1* embryos, this always precedes the correction of DNA segregation defects (n=18/18). We next examined mitotic and central spindle disassembly. While spindle disassembly coincides with the end of furrow ingression in control embryos, it precedes the correction of DNA segregation defects in *ani-1;pig-1* embryos (n=11/12) (Video S4). In control embryos, the central spindle starts to lose its compact structure at the end of furrow ingression and central spindle remnants associate with the ingressing furrow to form the midbody (Figure 1C, Video S5A). In *ani-1;pig-1* embryos, the central spindle starts to disassemble before the correction of DNA segregation defects (n=21/22) (Figure 1C, Video S5B). Central spindle remnants sometimes associate with the closing cytokinetic ring (Video S 5C and legend) while some become fainter and cannot be detected anymore at the end of cytokinesis (Video S5D). In summary, the correction of DNA segregation defects in *ani-1;pig-1* embryos occurs late during the cell cycle, when the nuclear envelope has already reformed and the mitotic and central spindle have disassembled.

Importantly, this correction mechanism is not specific to *ani-1;pig-1* embryos. Similarly, increased myosin activity following depletion of the Rho GAPs RGA-3/4 results in furrow displacement and DNA segregation defects, which are then corrected (Figure 1D and legend, Video S6). Laser ablation of anaphase centrosomes also leads to the relative mispositioning of the mitotic spindle and cytokinetic furrow. Notably, although DNA segregation defects resulting from anterior and posterior centrosome ablations occur in the opposite direction, both can be corrected (Figure 1E-F and legend, Video S7). Altogether, those results show that DNA segregation defects due to furrow and/or spindle mispositioning can be corrected in different contexts.

### Correction of DNA segregation defects involves both nuclear and furrow displacement

To elucidate the mechanisms underlying this correction process, we first tracked nuclei and cytokinetic furrow positions. In control embryos, the two nuclei are displaced towards the poles of the embryo during and after cytokinesis while furrow position remains stable during ring closure (Figure 1A and 2A-C, Video S1). In *ani-1;pig-1* embryos, posterior nucleus displacement is similar to control embryos (Figure 2B) while the anterior nucleus moves faster and further (Figures 1A and 2A, Video S1). Furthermore, while the furrow initially moves towards the anterior, it is then displaced towards the posterior during the correction process (Figures 1A and 2C, Video S1). Notably, the opposite displacements of the anterior nucleus and the cytokinetic furrow occur concomitantly (Figure 2D). Similarly, opposite anterior nucleus and furrow movements occur when DNA segregation defects due to RGA-3/4 depletion or anterior centrosome ablations are corrected (Figure S1A-C,E, Videos S6, S7). Reverse displacements are observed following posterior centrosome ablation (Figure S1D-E, Video S7). Opposite DNA and furrow movements thus correct DNA segregation defects due to furrow mispositioning.

### Nuclear microtubule interactions contribute to nuclear displacement

We next searched for the mechanisms involved in regulating nuclear displacement. We first tested the role of microtubules and used a thermosensitive allele (*zyg-12(or577)*) to inactivate the KASH protein ZYG-12 and prevent nuclei/microtubule interactions during the last steps of mitosis (Figure 3A and legend). This strongly inhibits anterior nuclear displacement in control embryos (Figure 3B) but only moderately affects anterior nuclear displacement in *ani-1;pig-1* embryos (Figure 3C). Moreover, it does not prevent DNA segregation defect correction (16/16 *ani-1;pig-1* and 13/14 *zyg-12;ani-1;pig-1* embryos with corrected DNA segregation defects). Hence, while nuclear/microtubule interactions are critical to move nuclei away from the cytokinetic furrow in control embryos, they are involved but not essential for anterior nuclear displacement in *ani-1;pig-1* embryos.

### Myosin activity regulates both nuclear and furrow displacement

We next looked for an additional mechanism that could participate in anterior nucleus displacement and tested the possible involvement of myosin by using a thermosensitive allele of non-muscle myosin-2 (*nmy-2(1490)*). *nmy-2;ani-1;pig-1* embryos were initially grown at permissive temperature to ensure that the increase in myosin activity due to the lack of PIG-1 and ANI-1 is sufficient to induce furrow mispositioning. They were then shifted at restrictive temperature 220 seconds after anaphase onset. In control embryos, myosin inactivation moderately reduces nuclear displacement (Figure 4A) and does not enhance the effect of ZYG-12 inactivation (Figure 4C). Thus, contrary to nuclear/microtubule interactions, myosin has a minor role in the regulation of nuclear position in control embryos. Myosin inactivation also moderately inhibits anterior nuclear displacement in *ani-1;pig-1* embryos (Figure 4B). By contrast, simultaneous inactivation of ZYG-12 and myosin severely reduces the efficiency of DNA segregation defect correction (correction in 12/12 *nmy-2;ani-1;pig-1* and 11/20 *nmy-2;zyg-12;ani-1;pig-1* embryos) (Figure 4D). Furthermore, anterior nucleus displacement is strongly impaired, both in rescued and non-rescued *nmy-2;zyg-12;ani-1;pig-1* embryos (Figure 4D). Altogether, our results demonstrate that microtubules and myosin independently contribute to the positioning of the anterior nucleus during the correction of DNA segregation defects in *ani-1;pig-1* embryos.

Importantly, we also found that myosin inactivation prevents the furrow from moving back towards the posterior in *nmy-2;ani-1;pig-1* embryos (Figure 4E-F, Video S8). Myosin therefore plays a crucial role in the correction process by concomitantly regulating nuclear and furrow displacements.

### Variations of myosin levels entail changes in cortical tension

Considering the importance of myosin in the correction process, we carefully examined myosin cortical levels. Anterior myosin cortical level briefly increases in control anaphase embryos while an excessive and long-lasting accumulation of myosin is observed in *ani-1;pig-1* embryos (Figure 5A, left) [13]. This accumulation slowly drops off during the correction process (Figure 5A, left). Those changes are specific to the anterior cortex, as myosin posterior cortical levels only weakly and briefly increase in control and *ani-1;pig-1* embryos (Figure 5A, right). Those observations prompted us to assess possible changes in cortical tension by performing laser-induced cortical ablation [17,18] (Figure 5B; Video S9). In control embryos, cortical tension during anaphase is slightly higher at the anterior than at the posterior cortex (Figure 5C). While posterior cortical tension does not change significantly in *ani-1;pig-1* embryos, anterior cortical tension increases during anaphase before declining at the end of the rescue process (Figure 5C). All these variations in cortical tension are consistent with the changes in myosin levels that we measured (Figure 5A).

### Changes in cortical myosin levels contribute to the repositioning of the nascent furrow

Cortical tension imbalance and asymmetric myosin-driven contraction of the cortex can alter daughter cell size in dividing Hela cells [19]. Variations in myosin level and cortical tension could thus explain furrow movements in *ani-1;pig-1* embryos. Consistent with this hypothesis, movement of the nascent furrow (ring diameter > 15 µm) is correlated with cortical myosin levels: large differences of myosin levels between the anterior and posterior cortex (Δmyosin > 50 a.u.) are associated with the initial anterior displacement of the nascent furrow while weaker differences (Δmyosin < 30 a.u.) coincide with the furrow starting to move back towards the posterior pole (Figure 6A).

If this correlation results from the mechanical action of cortical myosin on the furrow, we reasoned that furrow speed must be affected by factors that influence the mechanical resistance to furrow movements. Forces resisting furrow displacement include the resistance of the cortex itself, $F_{\mathrm{cort}}$, and the drag force exerted by the cytoplasm, $F_{\mathrm{cyt}}$ (Figure 6B). As the embryo is confined in its eggshell, the cytoplasm indeed needs to flow through the cytokinetic ring to allow furrow displacement in the opposite direction. This latter resisting force is expected to increase when the cytokinetic ring closes. If the difference of cortical myosin concentration between anterior and posterior cortices, ΔM, drives furrow motion, we expect the velocity of the furrow to scale as $v \sim \Delta M\, r^4 /(\alpha r^4 + \beta\, R^2(R^2 - r^2)$, where $R$ is the cell radius and $r$ the cytokinetic ring radius (modelling details in STAR methods). This model predicts that for a given myosin difference furrow speed depends on cytokinetic ring closure (Figure 6C, red continuous line (Δmyosin > 50 a.u)). The effect of myosin concentration imbalance will become negligible as the furrow closes (Figure 6C, compare red (Δmyosin > 50 a.u.) and black (Δmyosin < 30 a.u.) continuous lines; Figure 6D, compare green (ring diameter > 15 µm) and purple (ring diameter < 15 µm) continuous lines). In agreement with this model, for a given myosin difference furrow velocity strongly depends on cytokinetic ring opening (Figure 6C, red squares (Δmyosin > 50 a.u.)). Furthermore, the speed of the nascent furrow is correlated with myosin levels (Figure 6D, ring diameter > 15 µm, green squares and green dotted regression line) while this is not the case during furrow ingression (Figure 6D, ring diameter < 15 µm, purple dots and purple dotted regression line). Altogether, our data strongly suggest that changes in myosin cortical levels contribute to the displacement of the nascent cytokinetic furrow. However, as the cytokinetic ring closes, furrow movement is limited by the increasing cytoplasmic drag, suggesting the existence of a supplementary mechanism that contributes to further furrow displacement. Moreover, we observed a shift between the velocity of the furrow predicted by our model and our experimental data (Figure 6C-D). While the model predicts that myosin influences the speed of the furrow movement towards the anterior cortex, it does not account for the reverse movement of the furrow towards the posterior (Figure 6C-D, continuous lines) and a constant drift velocity must be added to our model to fit experimental data (Figure 6C-D, dashed lines, see STAR methods).

### Myosin-dependent cortical blebbing and cytoplasmic flow are associated with furrow displacement

We thus searched for additional mechanisms that could explain furrow repositioning. We first assessed the possible role of the central spindle. Inactivation of the central spindle protein SPD-1 during anaphase effectively disrupts the central spindle (Figure S2A) but does not inhibit either correction efficiency nor furrow displacement in *ani-1;pig-1* embryos (Figure S2B, Video S10A). Hence, the central spindle does not play an essential role in repositioning the furrow. This is consistent with our observations that the central spindle starts to disassemble before the correction process (Figure 1C, Video S5). We next tested whether nuclei could regulate cortical changes by controlling the localization of myosin regulators, similar to what was previously shown in *Drosophila* neuroblasts [20]. However, preventing nuclear reformation by depleting the nucleoporin NPP-8 (Figure S2C) does not prevent correction of DNA segregation defects or furrow displacement (Figure S2D and legend, Video S10B), indicating that nuclei do not control furrow repositioning through the sequestration of myosin regulators.

Notably, *ani-1;pig-1* embryos display strong cortical deformations, reminiscent of the blebs described in cultured cells [21,22]. Consistent with previous observations [21,23], cortical myosin level suddenly decreases at the site of bleb formation and then reappears at the edge of the bleb (Figure 7A, Video S11). Cortical blebs first arise at the posterior and anterior embryo poles (Figure 7A, t=128 sec, Video S11). They form early during anaphase, prior to or at the beginning of furrow ingression, when the furrow still moves towards the anterior pole of the embryo (Figure 7A-B, Video S11). About 250 seconds after anaphase onset, those posterior and anterior blebs cease and are replaced by blebs located on the anterior edge of the furrow (Figure 4E left, t=440 sec, 10/10 embryos, Figure 7A, t =300sec, Figure 7B, Videos S8 and S11). These latter blebs form during furrow ingression, appearing shortly prior to and then accompanying furrow posterior displacement (Figure 7A-B, Video S11). They do not form when myosin is inactivated (Figure 4E right, 11/11 embryos, Video S8). This suggests that bleb formation is due to the increased cortical tension measured in *ani-1;pig-1* embryos (Figure 5C), similar to what was previously shown in cultured cells [22,24]. Notably, blebs form in regions where the cortex is away from the eggshell and with the strongest cortical curvature (Figure 7A). Following the theory of bleb nucleation proposed in [22], we modelled the variation of free energy entailed by the nucleation of a bleb in the different regions of an embryo (modelling details in STAR methods). In agreement with our observations, this model predicts a higher probability of forming a bleb where the cortex is strongly curved.

Creation of new cortex by cortical blebs may contribute to the displacement of the nascent furrow by increasing the surface area of the blebbing daughter cell and thus relaxing its cortex. Moreover, as the furrow moves back towards the posterior, blebbing mostly occurs on the anterior edge of the furrow (Figure 7B) where it has the direct effect of locally displacing the base of the furrow (Videos S8 and S11); this may contribute to the correction of the nascent furrow position and add up to the effect of myosin decrease (Figure 7E). However, similar to what we have described for the effect of myosin concentration (see above), we expect that cortical relaxation and displacement of the base of the furrow is not sufficient to overcome the cytoplasmic drag force and to drive overall furrow displacement during ring closure.

Blebs can transiently reduce intracellular pressure and have been described to be associated with the appearance of cytoplasmic flow [23,24]. Interestingly, we observed local cytoplasmic flows directed towards cortical blebs in *ani-1;pig-1* embryos (Video S12). Thus, as blebs form on the anterior side of the furrow, the anterior daughter cell pressure decreases. When the cytokinetic ring narrows, we expect a comparatively slow pressure equilibration with the posterior daughter cell, driving in turn cytoplasmic flow. Indeed, posterior furrow displacement coincides with the appearance of a strong flow of cytoplasmic particles oriented towards the anterior pole of *ani-1;pig-1* embryos (Video S12). We used Particle Imaging Velocimetry (PIV) to quantify this flow and found that 75% of the measured velocity vectors are oriented towards the anterior in *ani-1;pig-1* embryos (speed < -25nm/s, n=13 embryos, Figure 7C). Such a flow is not observed in control embryos (only 30% of the velocity vectors with speed < -25nm/s, n=17, Video S12, Figure 7C) or when myosin is inactivated (39% of the velocity vectors with speed < -25nm/s, n=11, Figure 7D).

Finally, we observed that correction of furrow mispositioning resulting from RGA-3/4 depletion or anterior centrosome ablation is also associated with the formation of cortical blebs on the anterior side of the furrow and the appearance of an anteriorly directed cytoplasmic flow (Videos S6 and S7). Reversely, the correction of defects due to posterior centrosome ablation is associated with the formation of cortical blebs on the posterior side of the furrow and with a cytoplasmic flow directed towards the posterior (Video S7).

Altogether, our results strongly suggest that formation of cortical blebs on the side of the furrow locally releases pressure and induces a cytoplasmic flow towards low pressure areas. Since the embryo is confined in its eggshell, the flow of cytoplasmic material must then be compensated through the repositioning of the furrow in the opposite direction. It is thus very likely that cortical blebbing and the subsequent cytoplasmic flow contribute to furrow repositioning during ring closure (Figure 7E).

## Discussion

Our work shows that DNA segregation defects due to cytokinetic furrow mispositioning in one-cell *C. elegans* embryos can be corrected during late mitosis. This so far uncharacterized correction mechanism relies on opposite cytokinetic furrow and nucleus displacements and is accompanied by cortical blebbing and cytoplasmic flow. This mechanism is not specific to *ani-1;pig-1* embryos and is for instance also observed when the Rho GAPs RGA-3/4 are depleted or when relative spindle / furrow mispositioning is induced upon centrosome ablation.

Myosin plays a crucial role in the regulation of the different facets of the correction process. First, the different contractility of the anterior and posterior cortices exerts a pulling force on the nascent cytokinetic ring, oriented towards the more contractile end. In control embryos, this differential contractility remains low and is therefore not sufficient to displace significantly the furrow from the location imposed by mitotic spindle signalling (Figure 7E). On the contrary, the strong increase of anterior myosin levels in anaphase *ani-1;pig-1* embryos explains the initial shift of the nascent furrow towards the anterior cortex. The subsequent decrease of anterior myosin then slows down this movement. It can however not explain the repositioning of the furrow towards the posterior. Moreover, as the ring closes, the moving furrow behaves like a mechanical piston, which needs to displace cytoplasm to allow its own motion. Our theoretical model indicates that this creates a drag force, which is too large to be overcome by cortical contractility. Cortical blebs provide additional mechanisms, which contribute to furrow displacement both before and during cytokinetic ring closure. Formation of cortical blebs on the anterior side of the furrow leads to cortical expansion and contribute to the repositioning of the nascent furrow both by relaxing the actomyosin cortex and displacing the base of the furrow. A “depressuring effect” of cortical blebs and the subsequent cytoplasmic flow next displace the furrow when the cytokinetic ring closes (Figure 7E).

Our findings are reminiscent of what has previously been described in unconfined cultured cells [19]. Indeed, we find that excessive polar myosin contractility favours the risk of aneuploidy by mispositioning the cytokinetic furrow while cortical blebbing, which occurs in response to excessive cortical tension, contributes to the repositioning of the furrow, thereby helping to restore euploidy. In isolated cultured cells, variations in cortical tension induce changes in the Laplace force, which play a central role in cell shape regulation [19]. However, contrary to cultured cells, the one-cell *C. elegans* embryo is confined in a rigid eggshell. This restrains changes in cell curvature and creates a reaction force, which buffers changes in the Laplace force. Confinement thus creates geometrical constraints, which modulate the effects of cortical tension and the mechanisms involved in furrow repositioning. Moreover, our work highlights a new role for cortical blebs. Previous work suggested that blebs help providing more cortical surface and relaxing excessive pressure to stabilize cell shape during cell division [19]. Cortical expansion induced by cortical blebs also correct spindle mispositioning in anaphase Hela cells [23]. Those effects are similar to the effect of cortical blebs that we observe at the beginning of furrow ingression. However, we find that cortical blebs can also regulate the volume of each daughter cell through their “depressuring effect” when the dividing cell is in a confined environment. Intriguingly, cortical blebs also lead to the appearance of a cytoplasmic flow during correction of spindle mispositioning in anaphase Hela cells [23]. Whether this flow is also involved in the correction of spindle mispositioning would require further investigation.

In addition to its role in furrow repositioning, we found that myosin also regulates nuclear displacement. Notably, the anteriorly-directed movement of the nucleus and the flow of cytoplasmic particles occur simultaneously in *ani-1;pig-1* embryos. It is thus very likely that the cytoplasmic flow exerts a drag force on the anterior DNA to drive it through the cytokinetic ring. Remarkably, it was recently shown that regulation of myosin II activity is critical for proper nuclear movement during the cleavage divisions of *Drosophila* embryos. This effect of myosin also involves the regulation of cortical contractility and the appearance of cytoplasmic flows [25]. Finally, a supplementary and redundant mechanism based on nuclear/microtubule interactions also drives nuclear displacement – probably through the pulling of the nucleus by microtubules. The existence of these two mechanisms controlling nuclear displacement together with the coordination of furrow and nuclear displacements by the cytoplasmic flow are likely to increase the efficiency of DNA segregation defect correction (Figure 7E).

In conclusion, our work shows that dividing cells in a confined environment, as are most cells inside tissues, can benefit from a combination of rescue mechanisms, which prevents the polar actomyosin-driven destabilization of cytokinesis and can restore euploidy.

## Acknowledgments

We thank P. Askjaer, M. Delattre and the *Caenorhabitis* Genetics Center (funded by the National Institute of Health Office of Research Infrastructure Programs, P40 OD010440) for providing worm strains. We acknowledge W. Nahaboo and M. Delattre for sharing unpublished observations. M. Ponnavoy helped during the earlier steps of this project. N. Loyer and S. Prigent (Biogenouest, Université de Rennes 1) provided macros for tracking and PIV analysis. We thank S. Dutertre and X. Pinson (Microscopy Rennes Imaging Center, Biosit UMS 3480). S. Huet and M. Pinot advised us for laser ablation, L. Chesneau and A. Bidaud-Meynard for superresolution microscopy. Thanks to K. John, H. Bouvrais and J. Pécreaux for discussions and G. Charras for critical reading of the manuscript.

This work was supported by institutional funding from the Centre National de la Recherche Scientifique (CNRS) and Université Rennes 1. G. Michaux's team is supported by the Ligue Régionale contre le Cancer – Grand Ouest. J. Etienne is supported by the French National Research Agency ("Investissements d'avenir" program, ANR-15-IDEX-02, IRS "AnisoTiss"), acknowledges CNRS Momentum grant "Modeling of living systems", Tec21 (ANR-11-LABX-0030), and is member of GDR 3570 MécaBio and GDR 3070 CellTiss of CNRS.

## Author contributions

A.P. designed experiments with input from G.M. A.P and M.J. performed experiments. A.P., M.J. and J. E. analysed the data. J.E. performed biophysical modelling. A.P., J.E. and G.M. wrote the manuscript.

## Declaration of interests

The authors declare no competing interests.

## Main text Figure legends

**Figure 1. DNA segregation defects resulting from furrow mispositioning are corrected during late mitosis. A.** Furrow (arrow) and anterior nucleus (asterisk) positions during the division of control and *ani-1(RNAi);pig-1(gm344)* embryos. NMY-2::GFP labels non-muscle-myosin 2 and mCherry::HIS labels DNA. **B.** Nuclear envelope (labelled with EMR-1::mCherry) reformation in control and *ani-1(RNAi);pig-1(gm344)* embryos. **C.** Central spindle in control and *ani-1(RNAi);pig-1(gm344)* embryos. SPD-1::GFP labels the central spindle, centrosomes and nuclei after division [26], PH::GFP labels the membrane. Arrowhead indicates disassembled central spindle. **D.** *rga-3/4(RNAi)* embryos show DNA (asterisk) segregation defects (t=180 sec, 15/19 embryos), which are then corrected (t=250 sec, 13/15 embryos). **E-F.** Anterior (E) and posterior (F) centrosome ablation lead to spindle and/or furrow mispositioning and DNA segregation defects (17/18 and 16/30 embryos). Defects are corrected in 15/17 and 15/16 embryos. Embryos express NMY-2::GFP (cortical and furrow signals), GFP::α-tubulin (labels the centrosome and to a lesser extent microtubules) and GFP::HIS (DNA). Dashed circles indicate ablated centrosomes. Arrowheads point to anterior (E) or posterior (F) DNA and arrows to the furrow before the correction. Asterisk indicate nuclei position after division. In A and C-F: $t_0$ = anaphase onset. In B: $t_0$ = nuclear envelope breakdown. Scale bar: 10 µm. See also Videos S1-7.

**Figure 2. Correction of DNA segregation defects involves both nuclear and furrow displacement. A-B.** Average displacement of the anterior (A) and posterior (B) nuclei in control and *ani-1(RNAi);pig-1(gm344)* embryos. **C.** Average furrow tip position in control and *ani-1(RNAi);pig-1(gm344)* embryos **D.** Anterior nucleus and furrow tip position in a representative *ani-1(RNAi);pig-1(gm344)* embryo. See also Figure S1.

**Figure 3. Nuclear microtubule interactions contribute to nuclear displacement. A.** ZYG-12 inactivation prevents nuclei/microtubule interactions. In control (n=9) and *ani-1(RNAi);pig-1(gm344)* (n=12) embryos, centrosomes are closely juxtaposed to the nuclei on average 435 seconds after anaphase onset. In *zyg-12(or577)* embryos (n=9), centrosomes are never in close juxtaposition to the nuclei (embryos observed until the duplication of centrosomes preceding the second division). In *zyg-12(or577)*;*ani-1(RNAi);pig-1(gm344)* embryos (n=17), 14 embryos never showed juxtaposed centrosomes and nuclei while juxtaposition occurred very late (>500 sec after anaphase onset) in 3 embryos. In the embryos shown, posterior nuclei and most posterior centrosomes are out of focus. The second anterior centrosome is also out of focus in *ani-1;pig-1* and *zyg-12;ani-1;pig-1* embryos. $t_0$ = anaphase onset. Scale bar: 10 µm. **B-C.** Average displacement of the anterior nucleus in control, *zyg-12(or577), ani-1(RNAi);pig-1(gm344)* and *zyg-12(or577)*;*ani-1(RNAi);pig-1(gm344)* embryos.

**Figure 4. Myosin activity regulates both nuclear and furrow displacement**. **A-D.** Average displacement of the anterior nucleus in embryos of the indicated genotypes. In B and D, only embryos with corrected DNA segregation defects were analysed, except for *nmy-2(ne1490)*;*zyg-12(or577)*;*ani-1(RNAi);pig-1(gm344),* for which embryos with and without correction are presented separately. **E.** Furrow position in *ani-1(RNAi);pig-1(gm344)* and *nmy-2(ne1490)*;*ani-1(RNAi);pig-1(gm344)* embryos Asterisk indicates DNA. White dashed line indicates the most anterior position reached by the furrow. Arrowhead points to a cortical bleb on the anterior side of the furrow. Scale bar: 10 µm. **F.** Average furrow tip position in *ani-1(RNAi);pig-1(gm344)* and *nmy-2(ne1490)*;*ani-1(RNAi);pig-1(gm344)* embryos. Only embryos with corrected DNA segregation defects were analysed. Embryos did not show furrow regression during furrow tracking. See also Video S8.

**Figure 5. Variations in myosin concentration entail different levels of cortical tension. A.** Anterior (left) and posterior (right) cortical myosin levels in control and *ani-1(RNAi);pig-1(gm344)* embryos. **B.** Laser-induced ablation performed during anaphase at the anterior cortex of an *ani-1(RNAi);pig-1(gm344)* embryo. Images of the anterior cortex 0.5 sec before, 0.5 sec and 1.5 sec after ablation. White bar indicates the area targeted for ablation. Measurement of the ellipse small axis allowed us to determine the cut opening kinetics (see STAR methods). Scale bar: 5 µm. **C.** Initial opening velocities at the anterior and posterior cortex of control and *ani-1(RNAi);pig-1(gm344)* embryos. See also Video S9.

**Figure 6. Cortical myosin can reposition the nascent furrow. A.** Displacement of nascent cytokinetic furrows (ring diameter > 15 µm) depends on ΔMyosin. **B.** Model of the forces acting on furrow displacement. The stronger anterior cortical contractility exerts a pulling force on the nascent furrow ($F \sim \Delta M$) while resistance forces from the cortex ($F_{cort}$) and the cytoplasm ($F_{cyt}$) oppose to furrow displacement. *R:* cell radius, *r:* cytokinetic ring radius. **C.** Furrow velocity as a function of ring opening and myosin concentration. Black boxplots and red squares measurements correspond to low and high ΔM, respectively (n=89 for low ΔM and n=59 for high ΔM). The predicted velocity for low and high ΔM is represented by the solid black and red lines, respectively. A constant drift velocity needs to be added to the model (black and red dashed lines) to fit the experimental data. **D.** Furrow velocity as a function of myosin concentration and ring opening. Measured furrow velocity is correlated with ΔM in the case of nascent furrow (ring diameter > 15 µm, green squares and green dotted regression line) but not during ring closure (ring diameter < 15 µm, purple dots and purple dotted regression line). Predicted furrow velocity is represented without (solid lines) or with (dashed lines) addition of a constant drift, for a nascent furrow (ring diameter = 17 µm, green) or during ring closure (ring diameter = 12 µm, purple). In all panels, furrow velocity was measured between 300 sec and 450 sec after anaphase onset and time points were collected from 15 different embryos.

**Figure 7. Furrow repositioning is accompanied by cortical blebbing and cytoplasmic flow. A.** Formation of cortical blebs on the anterior and posterior poles (t=128 sec, arrows) and on the anterior side of the cytokinetic furrow (t=300 sec, arrowheads) in a *ani-1(RNAi);pig-1(gm344)* embryo. $t_0$ = anaphase onset. Scale bar: 10 µm. **B.** Presence of blebs at the posterior and anterior poles of the embryos precede the formation of blebs close to the furrow. Time points were collected from 15 different embryos. **C-D.** Distribution of velocity vector intensities measured by PIV. Only embryos with corrected DNA segregation defects and not showing furrow regression during flow measurement were analysed. **E.** Model of the mechanisms driving furrow and nuclear positions in wildtype and *ani-1(RNAi);pig-1(gm344)* embryos. In wildtype embryos, the differential contractility between the anterior and posterior cortices is not sufficient to displace the furrow from the location imposed by mitotic spindle signalling. In *ani-1(RNAi);pig-1(gm344)* embryos, the strong increase of anterior myosin levels exerts a pulling force on the nascent cytokinetic ring, moving it towards the anterior cortex. The subsequent decrease of anterior myosin and cortical expansion due to blebbing reposition the nascent furrow. Once the furrow closes, cortical blebbing and the ensuing cytoplasmic flow drives the opposite displacement of the cytokinetic furrow and the anterior nucleus. Microtubules also contribute to the correction process by pulling on the anterior nucleus. See also Figure S2 and Videos S10-12.

# STAR Methods

## Lead contact and materials availability

Further information and requests for *C. elegans* strains generated in this study should be directed to and will be fulfilled by the Lead Contact, Anne Pacquelet (anne.pacquelet@univ-rennes1.fr).

## Experimental model and subject details

### Worm strains and culture

*C. elegans* strains were grown on agar plates containing NGM growth media and seeded with *E. coli* (OP50 strain). Worms were maintained at 20°C, except strains carrying thermosensitive mutations, which were kept at 15°C. A list of the strains used in this study and conditions used for each experiment are detailed in the Key Resources Table and in Table S1.

## Method details

### RNAi conditions

RNAi was performed by feeding worms with RNAi clones from the Ahringer-Source Bioscience library [27] on 1 mM or 3 mM IPTG plates. L4440 was used as a control in all RNAi experiments. The clone used for *rga-3/4* RNAi is primarily directed against *rga-3* but also targets *rga-4* [28]. In the case of double RNAi experiments, RNAi cultures were initially grown separately; *ani-1* RNAi was then mixed either with control (L4440) or *npp-8* cultures (1:1) before seeding plates. Conditions used for each experiment are detailed in the Table S1.

### Time-lapse recordings

Embryos were mounted on 2% agarose pads in a drop of M9 medium. In most experiments, temperature was controlled using a temperature-control platform, which enables temperature shifts within 10 seconds (CherryTemp, Cherry Biotech). Conditions used for each experiment are detailed in Table S1.

To analyse the behaviour of the central spindle during the correction process, we first recorded the SPD-1::GFP signal during the whole division process. This experiment was used to quantify the number of embryos in which the central spindle already started to disassemble at the time of correction. To further characterize what happens to central spindle remnants, we first imaged embryos with DIC during the first steps of the division and then recorded the SPD-1::GFP signal at the end of the correction process. This allowed us to reduce photobleaching and thereby to better observe and quantify central spindle remnant behaviour when the cytokinetic ring closes.

Myosin inactivation was performed using a *nmy-2* thermosensitive allele. Previous work has shown that myosin inactivation leads to furrow regression and cytokinesis failure [29]. However, the effect of myosin inactivation is not immediate and the cytokinetic furrow can continue its ingression for several minutes before it starts regressing [29]**.** Based on these observations, we used temperature shift conditions (see Table S1) under which most embryos did not show furrow regression during the time course of experiments. One embryo showed furrow regression during cytoplasmic flow measurement and was excluded from our analysis (Figure 7D). Embryos in which furrow regression occurred at later time points than the ones used in our quantifications were kept for analysis.

### Chromosome imaging

Chromosomes labelled with mCherry::HIS-58 were imaged with a LSM 880 microscope (Zeiss), using a 63x oil-objective and the Fast Airy Scan module to obtain superresolution images. 480x480 pixel images were obtained at zoom 5.7, and speed 6.5 (155 ms per image). Z-stack were acquired with 300 nm steps.

### Centrosome ablations

Centrosome laser ablations were performed on a LSM 880 microscope (Zeiss) with a 355 nm pulsed-UV laser (Rapp Optoelectronic, 40% laser + ND1 filter, 10 iterations / ablation) and a 40x water-objective. A circular area encompassing the anterior or posterior centrosome was defined for each ablation. Ablation was performed during early anaphase. Images were recorded every 2 sec.

### Cortical ablations

Cortical laser ablations were performed on a LSM 880 microscope (Zeiss) with a 800 nm biphoton laser (Mai Tai, 50% power, 10 iterations / ablation) and a 63x oil-objective. A 0.17 x 6 µm rectangle perpendicular to the antero-posterior axis was used to define the cut area. The cut area was positioned on the anterior or posterior cortex, approximately at equal distance from the pole and the cytokinetic furrow. Ablations were performed during anaphase (1 min 10 sec to 1 min 50 sec after anaphase onset) or at the end of the correction process (5 to 8 min after anaphase onset). Images were recorded every 0.5 sec.

## Quantifications and statistical analysis

### Image analysis and quantifications

Images were assembled for illustration using ImageJ and Fiji. All embryos are oriented with anterior pole to the left. Position of the nuclei and of the furrow tip during ingression was tracked manually in ImageJ. Furrow tip position was measured starting at furrow ingression onset. Position is expressed as a percentage of embryo length, 0 and 100 correspond to the anterior and posterior pole of the embryos, respectively. Nuclei position tracking was generally started 100 sec after anaphase onset, when DNA separation due to anaphase spindle elongation is mostly finished. In Figure S2A, we started to measure anterior nucleus displacement at anaphase onset to be able to evaluate the effect of central spindle disassembly on DNA movement during anaphase. Nuclear displacement is expressed as a percentage of embryo length, positive and negative values correspond to a displacement towards the posterior and anterior pole of the embryos, respectively. Variations in experimental settings, in particular temperature shifts (see Table S1), explain the slight variations of nuclei or furrow dynamics observed between experiments for the same genotype.

Images of chromosomes obtained with the Fast Airy Scan module were processed to enhance resolution with the ZenBlack software. 3D reconstructions were then performed with the Imaris software.

Quantifications of myosin intensities (Figure 5A) were performed using ImageJ. A region corresponding to the most anterior or posterior 10–15% of the embryo cortex was defined and NMY-2::GFP cortical intensity was measured in a central confocal plane from anaphase onset to cytokinesis ring closure.

Furrow speed (Figure 6 and Figure 7B) was quantified based on furrow position by a LOESS regression over 4 time points. Time points were collected from 15 different *ani-1;pig-1* embryos with corrected DNA segregation defects. Positive and negative values of furrow velocity correspond to a displacement towards the posterior and anterior pole of the embryos, respectively. In Figure 6, analysis was restricted to a time window (300 sec to 450 sec after anaphase onset), during which both nascent (ring diameter > 15 µm) and closing (ring diameter < 15 µm) furrows coexist. All analysed time points are shown on plots, *t*-test and regression test are performed on subsamples for which velocities are calculated from disjoint time windows.

## Cortical tension measurement

Analysis of cortical ablation experiments was performed by drawing an ellipse fitting the opening area (see Figure 5B) as previously described [18,30]). Opening kinetics was analysed by measuring the increase of the ellipse minimum axis length following ablation. Cortical tension has been shown to be proportional to the velocity of cortex displacement which immediately follows ablation [17]. Here, the initial opening velocity was calculated by measuring the increase of the ellipse minimum axis between the first (0.5 sec) and third (1.5 sec) images taken after laser ablation.

## Flow measurement

Particle Imaging Velocimetry (PIV) was used to measure cytoplasmic flows in strains expressing VIT-2::GFP to label yolk particles. PIV analysis was performed with the Matlab MPIV toolbox and the Minimum Quadric Differences algorithm. Images were analysed using interrogation windows of 32*32 pixels with 50% overlap. Measurements were performed in the furrow region during the last 100 seconds of furrow closure. Frames in which nucleus displacement may have influenced the calculation of cytoplasmic flow were excluded from the analysis. Intensities of the velocity vectors along the embryo antero-posterior axis were calculated; positive and negative values correspond to a flow towards the posterior and anterior pole of the embryos, respectively. The distribution of the measured vector intensities was then determined for each embryo and finally averaged among all observed embryos.

**Modelling forces acting on furrow position**

Assuming that cortical myosin results in a force $F$ acting on the furrow and proportional to the difference of myosin concentration between anterior and posterior cortices, $\Delta M$, this force needs to be balanced with forces resisting furrow displacement (Figure 6B). Part of these forces are due to the resistance of the cortex itself ($F_{cort}$), this can be assumed proportional to furrow velocity $v$, and can be modelled as $-\alpha v$ (Figure 6B). Another resistance to furrow motion is the drag force exerted by the cytoplasm ($F_{cyt}$), which, due to confinement, needs to flow through the cytokinetic ring in order to allow displacement of the furrow in the opposite direction (Figure 6B). This drag force will be equal to the dynamic pressure difference on each side of the furrow times the section area of the furrow, $R^2-r^2$, where $R$ is the cell radius and $r$ the cytokinetic ring radius. Assuming a Poiseuille flow, the dynamic pressure drop will scale as $vR^2/r^4$. The cytoplasmic drag force can thus be modelled as $-\beta (R^2-r^2) vR^2/r^4$. Finally, the equilibrium between the force exerted by myosin and the forces resisting furrow displacement can be expressed as $F \sim \alpha v + \beta (R^2-r^2) vR^2/r^4$. Hence, the furrow velocity will scale as $v \sim \Delta M r^4 / (\alpha r^4 + \beta R^2 (R^2-r^2))$, which we plot in Figures 6C and 6D. One aspect of the data not captured in this model is a drift velocity seemingly independent from both myosin and furrow opening, and which may be ascribed to another biological control of furrow positioning (e.g. local signalling of myosin recruitment and/or effect of blebs and cytoplasmic flow) adding up to the balance. When adding a constant drift velocity to the above model, adjusting the two parameters $\alpha$ and $\beta$ allows to fit experimental datasets in the four curves shown in Figures 6C and 6D. In those conditions, we find that $\alpha/\beta=0.03$, indicating that cytoplasmic drag dominates other friction sources.

**Modelling bleb appearance probability**

Following [22], we write the variations of free energy entailed by the nucleation of a bleb of height $\delta$ by the detachment from the cortex of a patch of membrane of radius $a$ :

$$\Delta U = J\,a^2 - \Delta p\,a^2\,\delta + \mathrm{T}\,\delta^2$$

where $J$ is the membrane-cytoskeleton energy of adhesion, $\Delta p$ the pressure jump across membrane, $T$ the membrane tension; we have neglected bending energy.

In [22], the pressure jump is considered a uniform constant, since the cell is spherical and unconfined. In the present case, the confinement force adds up with the Laplace force and imposes a local curvature which is equal to the eggshell one (in locations where membrane is aposed to the eggshell) or larger than the eggshell one (at the furrow and at the poles when not in contact with eggshell). In these regions we have $\Delta p = 2\sigma/R$, where $\sigma$ is the cortical tension and $R$ the local characteristic radius of curvature. The lowest energy barrier to nucleate a bleb is at the saddle-point $\delta^*=JR/\sigma$, $a^*= (2\mathrm{TJ})^{1/2}\mathrm{R}/\sigma$, and is $\Delta U = TJR/\sigma$. For a given cortical tension, the regions with smaller $R$ (more curved) are thus more likely to nucleate blebs.

### Statistical analysis

Statistical analysis and graphic representations were performed with Excel and RStudio softwares. n corresponds to the number of analysed embryos except in Figure 6 where n corresponds to the number of time points used to measure furrow velocity (times points collected from 15 different embryos). Error bars represent standard deviation. Boxplots from Figure 5C and Figure 6A: central rectangles span the first to the third quartile of the data, middle lines correspond to median values, lower and higher whiskers to the minimum and maximum value, respectively. Figure 5C: two-tailed non parametric Wilcoxon tests were performed (data did not pass the Shapiro normality test). Figure 6A: a two-tailed unpaired Student's t test was performed (data passed the Shapiro normality tests and sample variance was equal).

## Data and code availability

This study did not generate any unique datasets or code.

## Legend for supplemental videos

**Video S1. Correction of DNA segregation defects resulting from furrow mispositioning in *ani-1;pig-1* embryos. Related to Figure 1.** Control (left) and *ani-1(RNAi);pig-1(gm344)* (right) embryos expressing NMY-2::GFP (magenta) and mCherry::HIS (yellow). Increased myosin levels at the anterior cortex of *ani-1(RNAi);pig-1(gm344)* embryos lead to furrow mispositioning and DNA segregation defects which are corrected late during mitosis. In control embryos the anterior nucleus (yellow asterisk) is slightly displaced during cytokinesis and furrow position remains stable (arrow). Correction in *ani-1(RNAi);pig-1(gm344)* embryos involves the strong displacement of the anterior nucleus (yellow asterisk) to the anterior and the displacement of the furrow (arrow) to the posterior. $t_0$ = anaphase onset. Images were recorded at 4 sec intervals and videos are played at 10 frames per second. Embryos are oriented with the anterior to the left. Scale bar: 10 µm.

**Video S2. 3D-reconstruction image of chromosomes in the anterior nucleus of a *ani-1;pig-1* embryo. Related to Figure 1.** *ani-1(RNAi);pig-1(gm344)* embryo expressing NMY-2::GFP (not shown) and mCherry::HIS (red, to label chromosomes). Scale bar: 2 µm.

**Video S3. Correction of DNA segregation defects in *ani-1;pig-1* embryos occurs after nuclear envelope reformation. Related to Figure 1.** Control (left) and *ani-1(RNAi);pig-1(gm344)* (right) embryos expressing NMY-2::GFP (magenta) and EMR-1::mCherry (yellow). Nuclear envelope reassembles before the correction of DNA segregation defects. $t_0$ = nuclear envelope breakdown. Images were recorded at 5 sec intervals and videos are played at 10 frames per second. Embryos are oriented with the anterior to the left. Scale bar: 10 µm.

**Video S4. Correction of DNA segregation defects in *ani-1;pig-1* embryos occurs after mitotic spindle disassembly. Related to Figure 1.** Control (left) and *ani-1(RNAi);pig-1(gm344)* (right) embryos expressing α-tubulin::YFP (magenta in upper images, gray in lower images) and mCherry::HIS (yellow in upper images). The mitotic spindle starts disassembling before the correction of DNA segregation defects. $t_0$ = anaphase onset. Images were recorded at 5 sec intervals and videos are played at 10 frames per second. Embryos are oriented with the anterior to the left. Scale bar: 10 µm.

**Video S5. Correction of DNA segregation defects in *ani-1;pig-1* embryos occurs after central spindle disassembly. Related to Figure 1. A-D.** Control (A) and *ani-1(RNAi);pig-1(gm344)* (B-D) embryos expressing SPD-1::GFP (magenta, labels the central spindle, centrosomes and the nuclei after division), PH::GFP (magenta, membrane labelling) and mCherry::HIS (yellow, not shown in C-D). The central spindle starts disassembling before the correction of DNA segregation defects (B). Note that central spindle remnants can be displaced towards the anterior by the cytoplasmic flow (B, 13/24 embryos) or stay in the posterior cytoplasm (D, 11/24 embryos). In some embryos, we observed that some central spindle remnants associate with the closing cytokinetic ring (C, arrowhead, 8/24 embryos). In others, no central spindle remnants could be observed at the time of ring closure (D, 14/24 embryos). In A-B, the SPD-1::GFP signal was imaged during the whole division process. $t_0$ = anaphase onset. Images were recorded at 5 sec intervals. In C-D, the SPD-1::GFP signal was imaged only at the end of the correction process (see STAR method for details). $t_0$ = cytokinetic ring closure. Images were recorded at 10 sec intervals. All videos are played at 10 frames per second. Embryos are oriented with the anterior to the left. Scale bar: 10 µm.

**Video S6. Correction of DNA segregation defects resulting from furrow mispositioning in *rga-3/4* embryos. Related to Figure 1.** Control (left) and *rga-3/4(RNAi)* (right) embryos expressing NMY-2::GFP (magenta) and mCherry::HIS (yellow). Increased myosin levels at the anterior cortex of *rga-3/4(RNAi)* embryos lead to furrow mispositioning and DNA segregation defects, which are corrected late during mitosis. Correction involves the opposite displacement of the anterior nucleus (yellow asterisk) and the furrow (white arrow) towards the anterior and posterior pole of the embryo, respectively. Cortical blebbing is first observed at the pole of the embryo (magenta arrow, 11/13 embryos) then on the anterior side of the furrow (magenta arrowheads, 12/13 embryos). Cytoplasmic flow is directed towards the anterior pole of the embryo (white arrowhead, 13/13 embryos). $t_0$ = anaphase onset. Images were recorded at 2 sec intervals and videos are played at 10 frames per second. Embryos are oriented with the anterior to the left. Scale bar: 10 µm.

**Video S7. Correction of DNA segregation defects following centrosome ablations. Related to Figure 1.** Ablation of anterior (left) or posterior (right) centrosome (white circle) in embryos expressing NMY-2::GFP (green, cortical and furrow signals), GFP::α-tubulin (green, labels the centrosome and to a lesser extent microtubules) and GFP::HIS (green, labels the DNA). The lower panel shows DIC recordings of the same embryos. Centrosome ablation leads to spindle and/or furrow mispositioning. Correction of the resulting DNA segregation defects involves both nucleus (asterisk) and furrow (arrow) displacement. In the case of anterior centrosome ablation (left), the anterior nucleus moves to the anterior and the furrow to the posterior of the embryo. Reversely, in the case of posterior centrosome ablation (right), the posterior nucleus moves to the posterior and the furrow to the anterior of the embryo. Cortical blebbing (arrowheads) and cytoplasmic flow (arrows) can be observed on DIC images. In the case of anterior centrosome ablation (left), cortical blebs form on the anterior side of the furrow (13/15 embryos) and an anteriorly directed flow is observed (15/15 embryos). In the case of posterior centrosome ablation (right), cortical blebs form on the posterior side of the furrow (14/15 embryos) and an anteriorly directed flow is observed (14/15 embryos). $t_0$ = anaphase onset. Images were recorded at 2 sec intervals and videos are played at 10 frames per second. Embryos are oriented with the anterior to the left. Scale bar: 10 µm.

**Video S8. Myosin activity controls furrow displacement. Related to Figure 4.** *ani-1(RNAi);pig-1(gm344)* (left) and *nmy-2(ne1490)*;*ani-1(RNAi);pig-1(gm344)* (right) embryos expressing GFP::PH (magenta) and mCherry::HIS (yellow, anterior nucleus also marked with asterisk). During correction, the furrow is displaced towards the posterior in *ani-1(RNAi);pig-1(gm344)* embryos but not in *nmy-2(ne1490)*;*ani-1(RNAi);pig-1(gm344)* embryos. In *ani-1(RNAi);pig-1(gm344)* embryos, furrow displacement is associated with cortical blebbing on the anterior side of the furrow (white arrowheads). Formation of those cortical blebs locally displaces the base of the furrow and leads to furrow inclination. $t_0$ = anaphase onset. Images were recorded at 2 sec intervals and videos are played at 10 frames per second. Embryos are oriented with the anterior to the left. Scale bar: 10 µm.

**Video S9. Laser-induced cortical ablation. Related to Figure 5.** Ablation of the anterior cortex of a *ani-1(RNAi);pig-1(gm344)* embryo was performed during anaphase. The embryo expresses NMY-2::GFP (green) and mCherry::HIS (not shown). White bar indicates the area targeted for laser ablation. Video starts 3 sec before laser ablation. Images were recorded at 0.5 sec intervals and video is played at 10 frames per second. Scale bar: 5 µm.

**Video S10. SPD-1 inactivation and NPP-8 depletion do not prevent furrow displacement. Related to Figure 7 and Figure S2. A.** DIC recording of a *spd-1(oj5);ani-1(RNAi);pig-1(gm344)* embryo expressing NMY-2::GFP and mCherry::HIS (not shown). SPD-1 inactivation does not prevent cortical blebbing (arrowheads) or furrow displacement (arrow). $t_0$ = furrow ingression onset. Images were recorded at 2 sec intervals and Video S is played at 10 frames per second. **B.** *ani-1(RNAi);pig-1(gm344)npp-8(RNAi)* embryo expressing NMY-2::GFP (magenta) and mCherry::HIS (yellow). NPP-8 depletion does not prevent cortical blebbing (arrowheads) or furrow displacement (arrow). $t_0$ = furrow ingression onset. Images were recorded at 4 sec intervals and video is played at 5 frames per second. In A and B, embryos are oriented with the anterior to the left. Scale bar: 10 µm.

**Video S11. *ani-1;pig-1* embryos display strong cortical blebbing. Related to Figure 7.** DIC (left) and GFP (right) images of a *ani-1(RNAi);pig-1(gm344)* embryo expressing NMY-2::GFP (gray, right images) and mCherry::HIS (not shown). Cortical blebs first form both at the posterior and anterior cortical poles (arrows) and then on the anterior side of the cytokinetic furrow (arrowheads). They are characterized by a transient decrease in cortical myosin level (images on the right). Formation of cortical blebs close to the furrow (arrowheads) locally displaces the base of the furrow and leads to furrow inclination. $t_0$ = anaphase onset. Images were recorded at 4 sec intervals and videos are played at 10 frames per second. Embryo is oriented with the anterior to the left. Scale bar: 10 µm.

**Video S12. Correction of DNA segregation defects in *ani-1;pig-1* embryos is associated with strong cytoplasmic flow. Related to Figure 7.** Control (left) and *ani-1(RNAi);pig-1(gm344)* (right) embryos expressing VIT-2::GFP (green). A strong flow of cytoplasmic particles directed towards the anterior pole is observed during the correction of DNA segregation defects in *ani-1(RNAi);pig-1(gm344)* embryos. A local flow directed towards the bleb that forms next to the furrow is also shown (arrow). $t_0$ = cytokinetic ring closure. Images were recorded at 1 sec intervals and videos are played at 10 frames per second. Embryos are oriented with the anterior to the left. Scale bar: 10 µm.

## References

1. Bringmann, H., and Hyman, A.A. (2005). A cytokinesis furrow is positioned by two consecutive signals. Nature *436*, 731–734.

2. Dechant, R., and Glotzer, M. (2003). Centrosome separation and central spindle assembly act in redundant pathways that regulate microtubule density and trigger cleavage furrow formation. Dev. Cell *4*, 333–344.

3. Basant, A., Lekomtsev, S., Tse, Y.C., Zhang, D., Longhini, K.M., Petronczki, M., and Glotzer, M. (2015). Aurora B kinase promotes cytokinesis by inducing centralspindlin oligomers that associate with the plasma membrane. Dev. Cell *33*, 204–215.

4. Nishimura, Y., and Yonemura, S. (2006). Centralspindlin regulates ECT2 and RhoA accumulation at the equatorial cortex during cytokinesis. J. Cell Sci. *119*, 104–114.

5. Yüce, O., Piekny, A., and Glotzer, M. (2005). An ECT2-centralspindlin complex regulates the localization and function of RhoA. J. Cell Biol. *170*, 571–582.

6. Bringmann, H., Cowan, C.R., Kong, J., and Hyman, A.A. (2007). LET-99, GOA-1/GPA-16, and GPR-1/2 are required for aster-positioned cytokinesis. Curr. Biol. CB *17*, 185–191.

7. Lewellyn, L., Dumont, J., Desai, A., and Oegema, K. (2010). Analyzing the effects of delaying aster separation on furrow formation during cytokinesis in the Caenorhabditis elegans embryo. Mol. Biol. Cell *21*, 50–62.

8. Mangal, S., Sacher, J., Kim, T., Osório, D.S., Motegi, F., Carvalho, A.X., Oegema, K., and Zanin, E. (2018). TPXL-1 activates Aurora A to clear contractile ring components from the polar cortex during cytokinesis. J. Cell Biol. *217*, 837–848.

9. Price, K.L., and Rose, L.S. (2017). LET-99 functions in the astral furrowing pathway, where it is required for myosin enrichment in the contractile ring. Mol. Biol. Cell *28*, 2360–2373.

10. Werner, M., Munro, E., and Glotzer, M. (2007). Astral signals spatially bias cortical myosin recruitment to break symmetry and promote cytokinesis. Curr. Biol. CB *17*, 1286–1297.

11. Cabernard, C., Prehoda, K.E., and Doe, C.Q. (2010). A spindle-independent cleavage furrow positioning pathway. Nature *467*, 91–94.

12. Ou, G., Stuurman, N., D'Ambrosio, M., and Vale, R.D. (2010). Polarized myosin produces unequal-size daughters during asymmetric cell division. Science *330*, 677–680.

13. Pacquelet, A., Uhart, P., Tassan, J.-P., and Michaux, G. (2015). PAR-4 and anillin regulate myosin to coordinate spindle and furrow position during asymmetric division. J. Cell Biol. *210*, 1085–1099.

14. Lara-Gonzalez, P., Westhorpe, F.G., and Taylor, S.S. (2012). The Spindle Assembly Checkpoint. Curr. Biol. *22*, R966–R980.

15. Norden, C., Mendoza, M., Dobbelaere, J., Kotwaliwale, C.V., Biggins, S., and Barral, Y. (2006). The NoCut pathway links completion of cytokinesis to spindle midzone function to prevent chromosome breakage. Cell *125*, 85–98.

16. Steigemann, P., Wurzenberger, C., Schmitz, M.H.A., Held, M., Guizetti, J., Maar, S., and Gerlich, D.W. (2009). Aurora B-mediated abscission checkpoint protects against tetraploidization. Cell *136*, 473–484.

17. Mayer, M., Depken, M., Bois, J.S., Jülicher, F., and Grill, S.W. (2010). Anisotropies in cortical tension reveal the physical basis of polarizing cortical flows. Nature *467*, 617–621.

18. Saha, A., Nishikawa, M., Behrndt, M., Heisenberg, C.-P., Jülicher, F., and Grill, S.W. (2016). Determining Physical Properties of the Cell Cortex. Biophys. J. *110*, 1421–1429.

19. Sedzinski, J., Biro, M., Oswald, A., Tinevez, J.-Y., Salbreux, G., and Paluch, E. (2011). Polar actomyosin contractility destabilizes the position of the cytokinetic furrow. Nature *476*, 462–466.

20. Montembault, E., Claverie, M.-C., Bouit, L., Landmann, C., Jenkins, J., Tsankova, A., Cabernard, C., and Royou, A. (2017). Myosin efflux promotes cell elongation to coordinate chromosome segregation with cell cleavage. Nat. Commun. *8*, 326.

21. Charras, G.T., Hu, C.-K., Coughlin, M., and Mitchison, T.J. (2006). Reassembly of contractile actin cortex in cell blebs. J. Cell Biol. *175*, 477–490.

22. Charras, G.T., Coughlin, M., Mitchison, T.J., and Mahadevan, L. (2008). Life and times of a cellular bleb. Biophys. J. *94*, 1836–1853.

23. Kiyomitsu, T., and Cheeseman, I.M. (2013). Cortical dynein and asymmetric membrane elongation coordinately position the spindle in anaphase. Cell *154*, 391–402.

24. Tinevez, J.-Y., Schulze, U., Salbreux, G., Roensch, J., Joanny, J.-F., and Paluch, E. (2009). Role of cortical tension in bleb growth. Proc. Natl. Acad. Sci. U. S. A. *106*, 18581–18586.

25. Deneke, V.E., Puliafito, A., Krueger, D., Narla, A.V., De Simone, A., Primo, L., Vergassola, M., De Renzis, S., and Di Talia, S. (2019). Self-Organized Nuclear Positioning Synchronizes the Cell Cycle in Drosophila Embryos. Cell *177*, 925-941.e17.

26. Nahaboo, W., Zouak, M., Askjaer, P., and Delattre, M. (2015). Chromatids segregate without centrosomes during Caenorhabditis elegans mitosis in a Ran- and CLASP-dependent manner. Mol. Biol. Cell *26*, 2020–2029.

27. Kamath, R.S., Fraser, A.G., Dong, Y., Poulin, G., Durbin, R., Gotta, M., Kanapin, A., Le Bot, N., Moreno, S., Sohrmann, M., *et al.* (2003). Systematic functional analysis of the Caenorhabditis elegans genome using RNAi. Nature *421*, 231–237.

28. Schmutz, C., Stevens, J., and Spang, A. (2007). Functions of the novel RhoGAP proteins RGA-3 and RGA-4 in the germ line and in the early embryo of C. elegans. Development *134*, 3495–3505.

29. Davies, T., Jordan, S.N., Chand, V., Sees, J.A., Laband, K., Carvalho, A.X., Shirasu-Hiza, M., Kovar, D.R., Dumont, J., and Canman, J.C. (2014). High-resolution temporal analysis reveals a functional timeline for the molecular regulation of cytokinesis. Dev. Cell *30*, 209–223.

30. Vuong-Brender, T.T.K., Ben Amar, M., Pontabry, J., and Labouesse, M. The interplay of stiffness and force anisotropies drives embryo elongation. eLife *6*. Available at: https://www.ncbi.nlm.nih.gov/pmc/articles/PMC5371431/ [Accessed December 7, 2018].

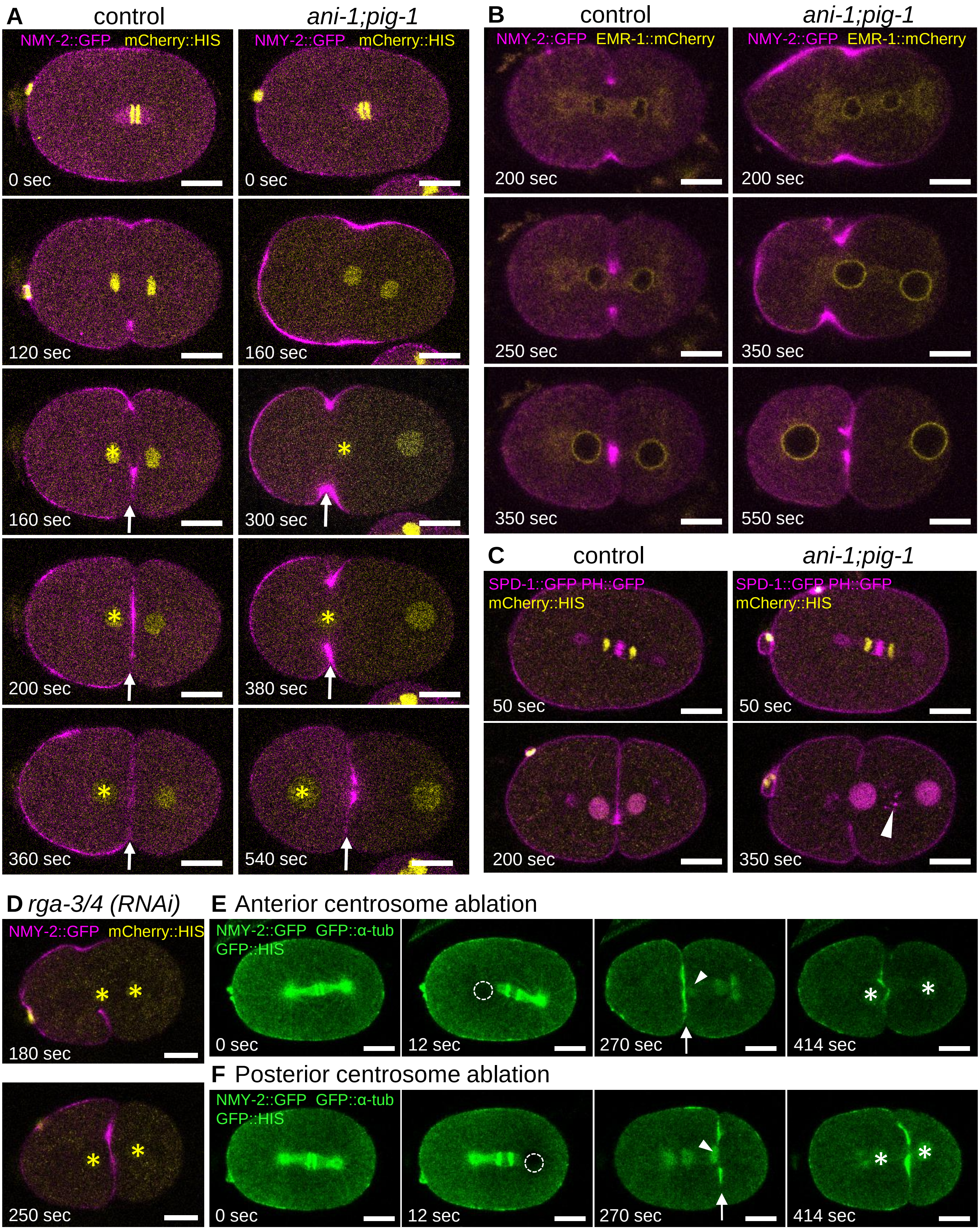
A
control
ani-1;pig-1
NMY-2::GFP mCherry::HIS
NMY-2::GFP mCherry::HIS
0 sec
0 sec
120 sec
160 sec
160 sec
300 sec
200 sec
380 sec
360 sec
540 sec
B
control
ani-1;pig-1
NMY-2::GFP EMR-1::mCherry
NMY-2::GFP EMR-1::mCherry
200 sec
200 sec
250 sec
350 sec
350 sec
550 sec
C
control
ani-1;pig-1
SPD-1::GFP PH::GFP mCherry::HIS
SPD-1::GFP PH::GFP mCherry::HIS
50 sec
50 sec
200 sec
350 sec
D rga-3/4 (RNAi)
NMY-2::GFP mCherry::HIS
180 sec
250 sec
E Anterior centrosome ablation
NMY-2::GFP GFP::α-tub GFP::HIS
0 sec
12 sec
270 sec
414 sec
F Posterior centrosome ablation
NMY-2::GFP GFP::α-tub GFP::HIS
0 sec
12 sec
270 sec
414 sec

Figure 1

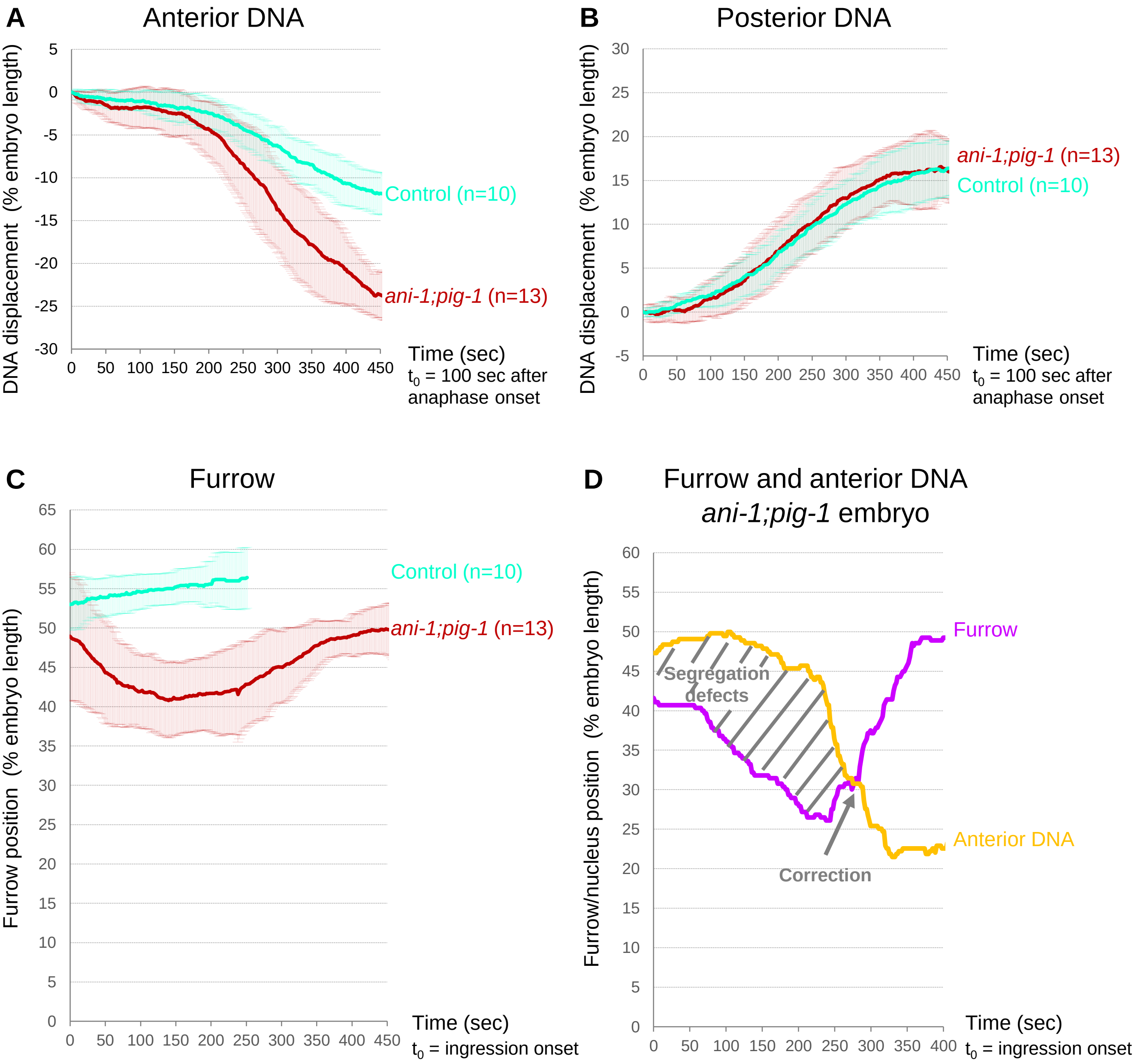
A
Anterior DNA
DNA displacement (% embryo length)
5
0
-5
-10
-15
-20
-25
-30
0 50 100 150 200 250 300 350 400 450
Control (n=10)
*ani-1;pig-1* (n=13)
Time (sec)
$t_0$ = 100 sec after anaphase onset
B
Posterior DNA
DNA displacement (% embryo length)
30
25
20
15
10
5
0
-5
0 50 100 150 200 250 300 350 400 450
*ani-1;pig-1* (n=13)
Control (n=10)
Time (sec)
$t_0$ = 100 sec after anaphase onset
C
Furrow
Furrow position (% embryo length)
65
60
55
50
45
40
35
30
25
20
15
10
5
0
0 50 100 150 200 250 300 350 400 450
Control (n=10)
*ani-1;pig-1* (n=13)
Time (sec)
$t_0$ = ingression onset
D
Furrow and anterior DNA
*ani-1;pig-1* embryo
Furrow/nucleus position (% embryo length)
60
55
50
45
40
35
30
25
20
15
10
5
0
0 50 100 150 200 250 300 350 400
Segregation defects
Furrow
Anterior DNA
Correction
Time (sec)
$t_0$ = ingression onset

Figure 2

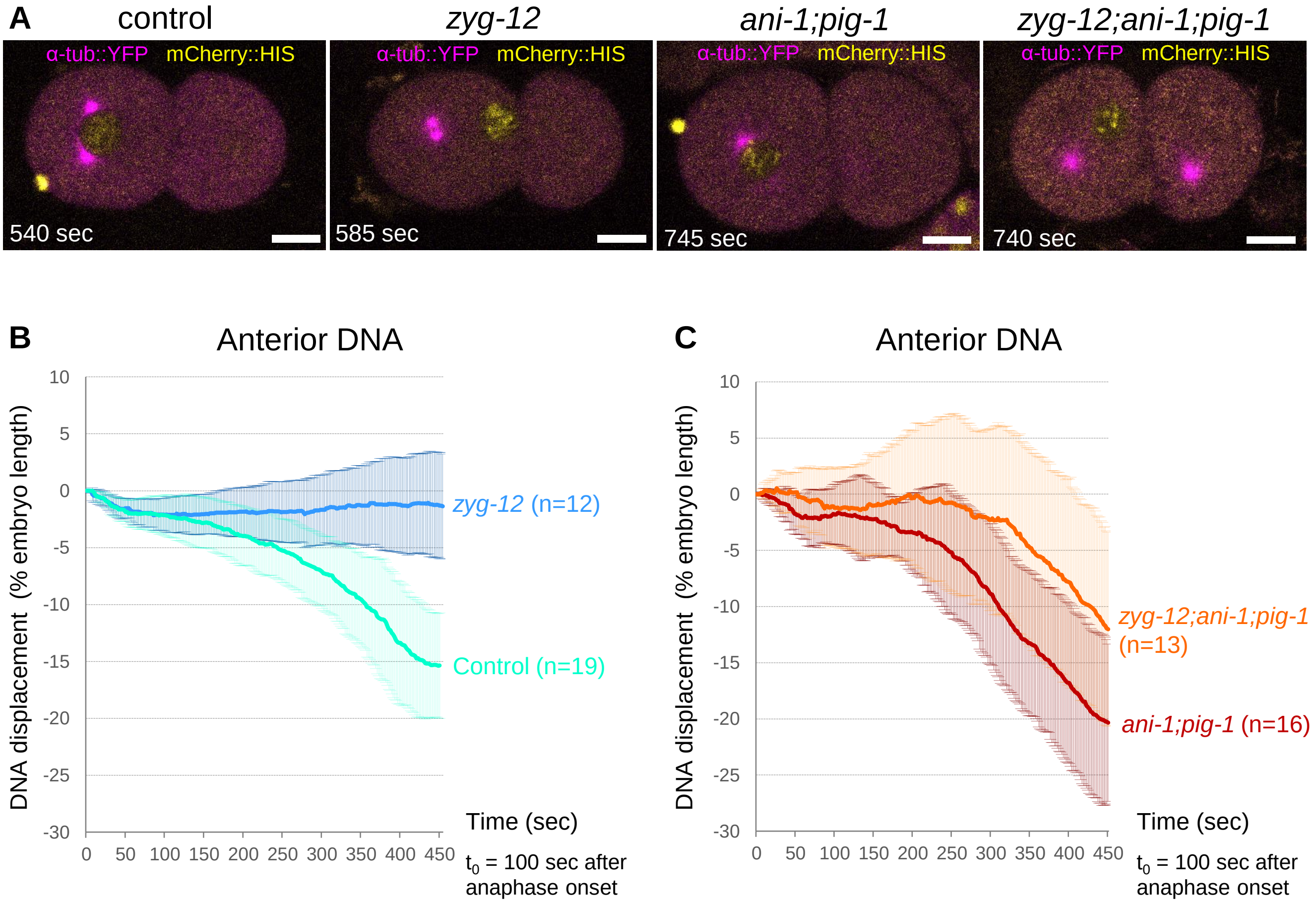
A
control
zyg-12
ani-1;pig-1
zyg-12;ani-1;pig-1
α-tub::YFP mCherry::HIS
540 sec
585 sec
745 sec
740 sec
B
Anterior DNA
DNA displacement (% embryo length)
10
5
0
-5
-10
-15
-20
-25
-30
0 50 100 150 200 250 300 350 400 450
zyg-12 (n=12)
Control (n=19)
Time (sec)
$t_0$ = 100 sec after anaphase onset
C
Anterior DNA
DNA displacement (% embryo length)
zyg-12;ani-1;pig-1 (n=13)
ani-1;pig-1 (n=16)
Time (sec)
$t_0$ = 100 sec after anaphase onset

Figure 3

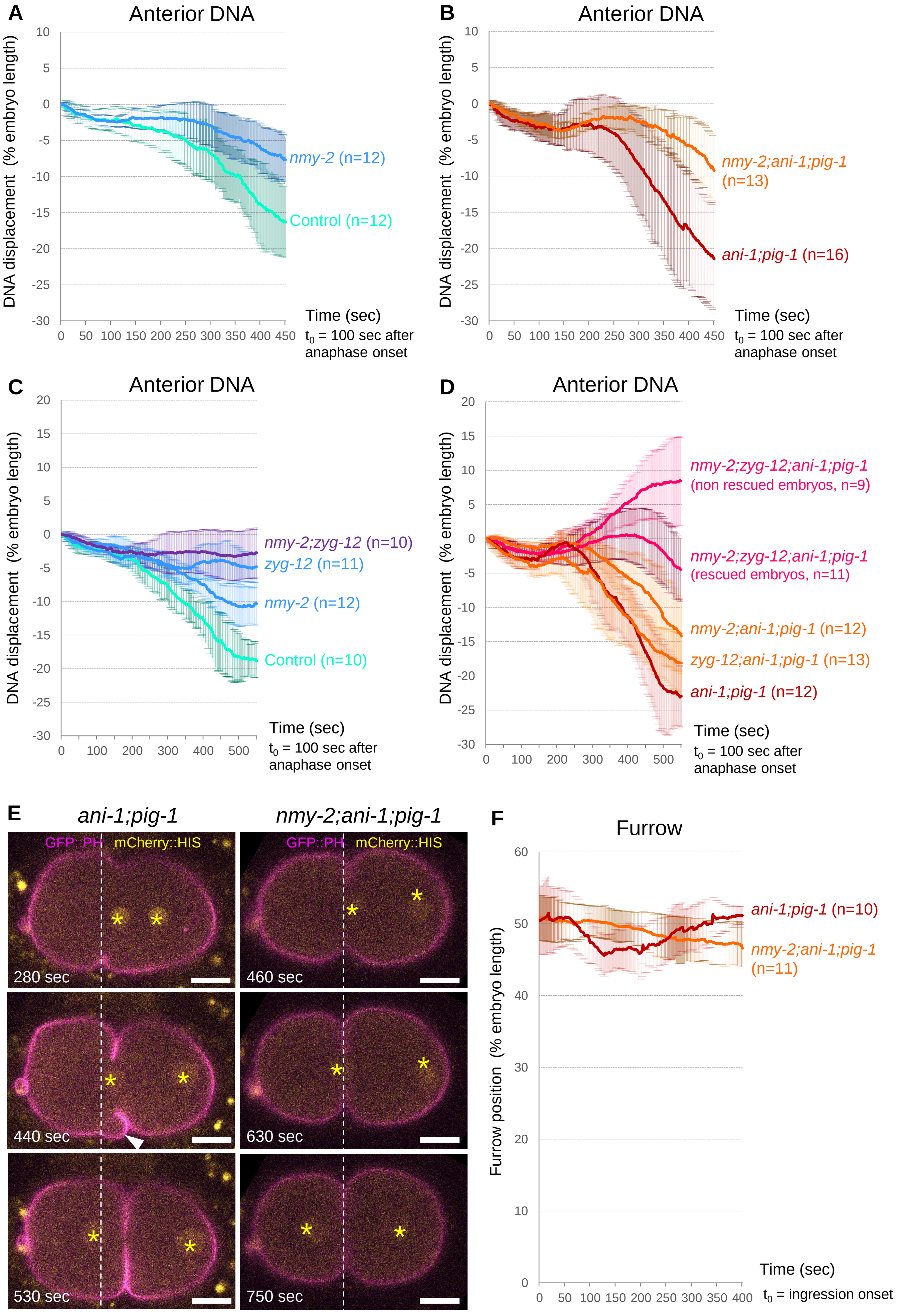
A
Anterior DNA
DNA displacement (% embryo length)
10
5
0
-5
-10
-15
-20
-25
-30
0 50 100 150 200 250 300 350 400 450
nmy-2 (n=12)
Control (n=12)
Time (sec)
t0 = 100 sec after anaphase onset
B
Anterior DNA
DNA displacement (% embryo length)
nmy-2;ani-1;pig-1 (n=13)
ani-1;pig-1 (n=16)
Time (sec)
t0 = 100 sec after anaphase onset
C
Anterior DNA
DNA displacement (% embryo length)
20
15
10
5
0
-5
-10
-15
-20
-25
-30
0 100 200 300 400 500
nmy-2;zyg-12 (n=10)
zyg-12 (n=11)
nmy-2 (n=12)
Control (n=10)
Time (sec)
t0 = 100 sec after anaphase onset
D
Anterior DNA
DNA displacement (% embryo length)
nmy-2;zyg-12;ani-1;pig-1 (non rescued embryos, n=9)
nmy-2;zyg-12;ani-1;pig-1 (rescued embryos, n=11)
nmy-2;ani-1;pig-1 (n=12)
zyg-12;ani-1;pig-1 (n=13)
ani-1;pig-1 (n=12)
Time (sec)
t0 = 100 sec after anaphase onset
E
ani-1;pig-1
nmy-2;ani-1;pig-1
GFP::PH mCherry::HIS
280 sec
440 sec
530 sec
460 sec
630 sec
750 sec
F
Furrow
Furrow position (% embryo length)
60
50
40
30
20
10
0
0 50 100 150 200 250 300 350 400
ani-1;pig-1 (n=10)
nmy-2;ani-1;pig-1 (n=11)
Time (sec)
t0 = ingression onset

Figure 4

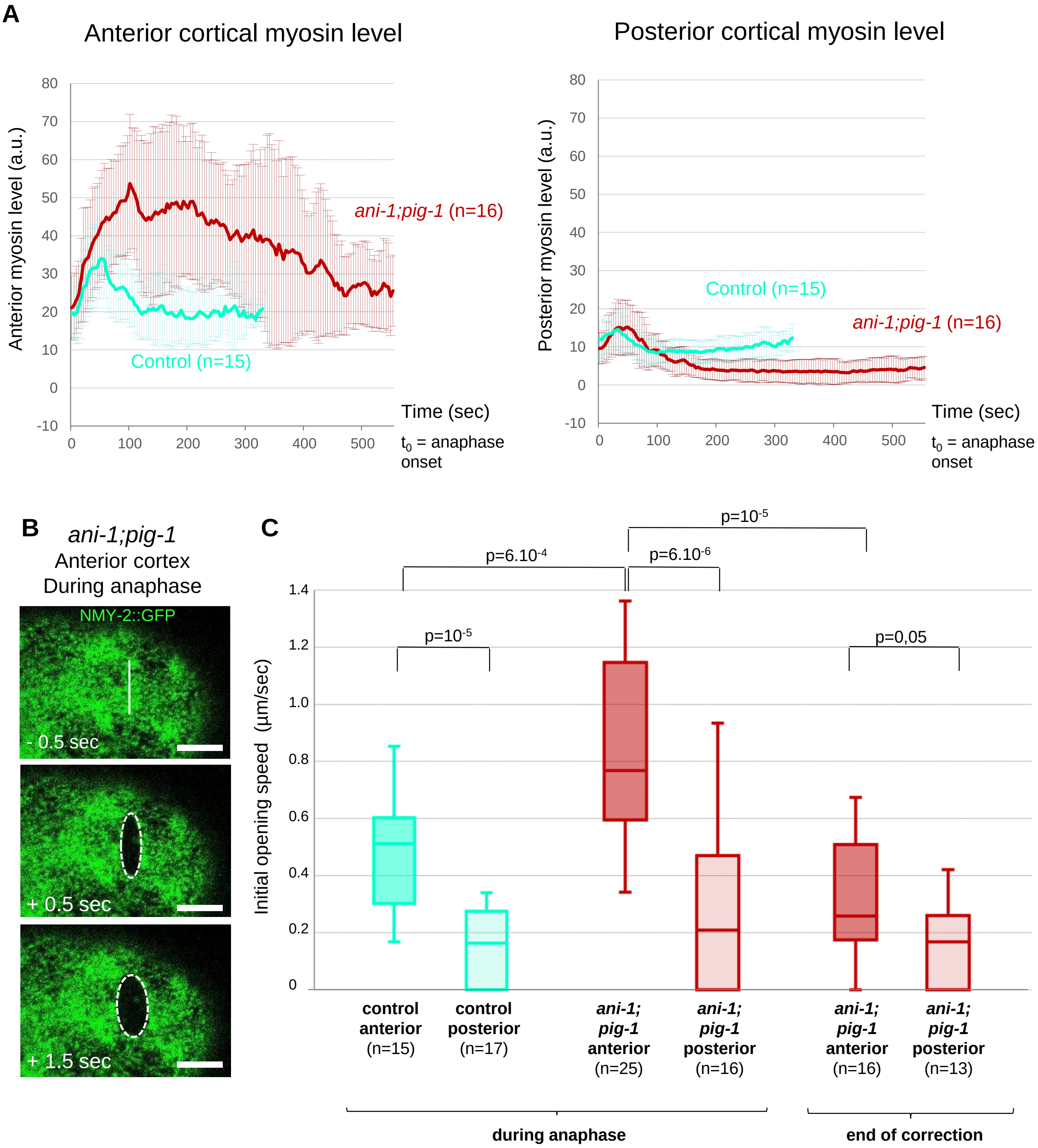
A
Anterior cortical myosin level
Anterior myosin level (a.u.)
80
70
60
50
40
30
20
10
0
-10
0
100
200
300
400
500
ani-1;pig-1 (n=16)
Control (n=15)
Time (sec)
t0 = anaphase onset
Posterior cortical myosin level
Posterior myosin level (a.u.)
80
70
60
50
40
30
20
10
0
-10
0
100
200
300
400
500
Control (n=15)
ani-1;pig-1 (n=16)
Time (sec)
t0 = anaphase onset
B
ani-1;pig-1
Anterior cortex
During anaphase
NMY-2::GFP
- 0.5 sec
+ 0.5 sec
+ 1.5 sec
C
p=10-5
p=6.10-4
p=6.10-6
p=10-5
p=0,05
Initial opening speed (µm/sec)
1.4
1.2
1.0
0.8
0.6
0.4
0.2
0
control anterior (n=15)
control posterior (n=17)
ani-1; pig-1 anterior (n=25)
ani-1; pig-1 posterior (n=16)
ani-1; pig-1 anterior (n=16)
ani-1; pig-1 posterior (n=13)
during anaphase
end of correction

Figure 5

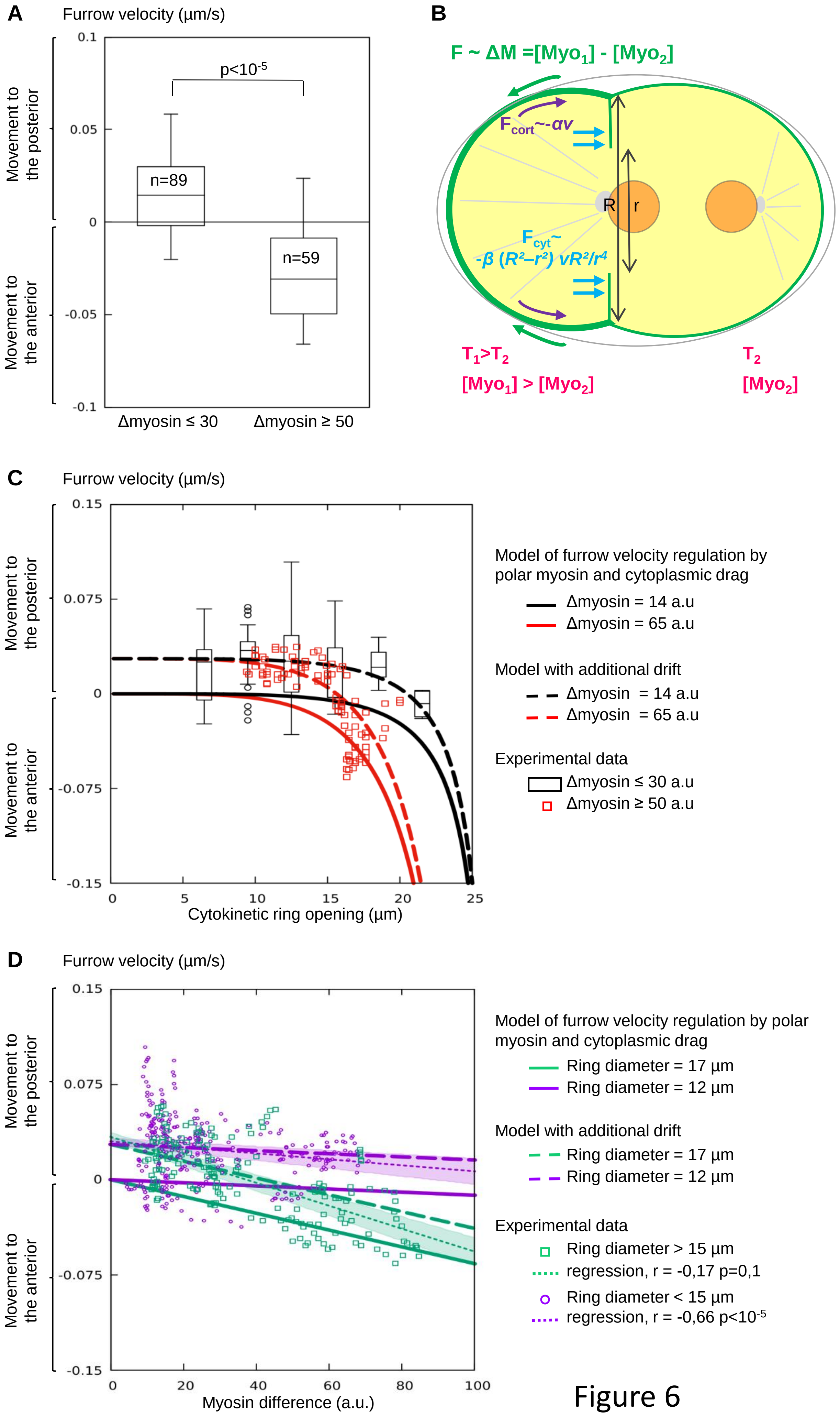
A
Furrow velocity (µm/s)
Movement to the posterior
Movement to the anterior
0.1
0.05
0
-0.05
-0.1
$p<10^{-5}$
n=89
n=59
Δmyosin ≤ 30
Δmyosin ≥ 50
B
F ~ ΔM =[Myo$_1$] - [Myo$_2$]
$F_{cort}$~-αv
$F_{cyt}$~ -β ($R^2$–$r^2$) v$R^2$/$r^4$
R
r
$T_1$>$T_2$
[Myo$_1$] > [Myo$_2$]
$T_2$
[Myo$_2$]
C
Furrow velocity (µm/s)
Movement to the posterior
Movement to the anterior
0.15
0.075
0
-0.075
-0.15
0
5
10
15
20
25
Cytokinetic ring opening (µm)
Model of furrow velocity regulation by polar myosin and cytoplasmic drag
Δmyosin = 14 a.u
Δmyosin = 65 a.u
Model with additional drift
Δmyosin = 14 a.u
Δmyosin = 65 a.u
Experimental data
Δmyosin ≤ 30 a.u
Δmyosin ≥ 50 a.u
D
Furrow velocity (µm/s)
Movement to the posterior
Movement to the anterior
0.15
0.075
0
-0.075
-0.15
0
20
40
60
80
100
Myosin difference (a.u.)
Model of furrow velocity regulation by polar myosin and cytoplasmic drag
Ring diameter = 17 µm
Ring diameter = 12 µm
Model with additional drift
Ring diameter = 17 µm
Ring diameter = 12 µm
Experimental data
Ring diameter > 15 µm
regression, r = -0,17 p=0,1
Ring diameter < 15 µm
regression, r = -0,66 $p<10^{-5}$

Figure 6

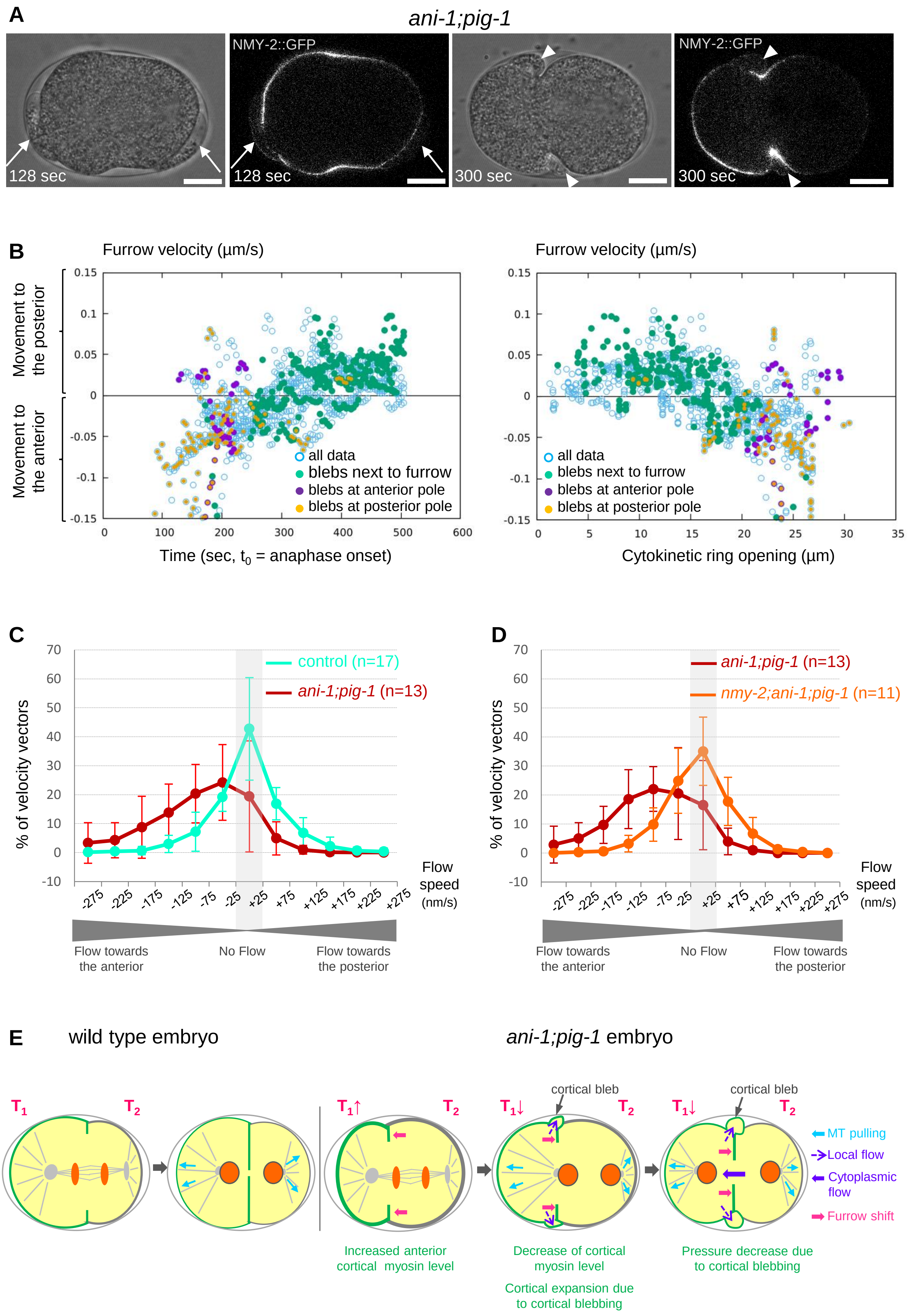
A
ani-1;pig-1
NMY-2::GFP
128 sec
128 sec
300 sec
NMY-2::GFP
300 sec
B
Furrow velocity (µm/s)
Movement to the posterior
Movement to the anterior
0.15
0.1
0.05
0
-0.05
-0.1
-0.15
0
100
200
300
400
500
600
Time (sec, $t_0$ = anaphase onset)
○ all data
● blebs next to furrow
● blebs at anterior pole
● blebs at posterior pole
Furrow velocity (µm/s)
0
5
10
15
20
25
30
35
Cytokinetic ring opening (µm)
C
% of velocity vectors
70
60
50
40
30
20
10
0
-10
control (n=17)
ani-1;pig-1 (n=13)
-275
-225
-175
-125
-75
-25
+25
+75
+125
+175
+225
+275
Flow speed (nm/s)
Flow towards the anterior
No Flow
Flow towards the posterior
D
% of velocity vectors
ani-1;pig-1 (n=13)
nmy-2;ani-1;pig-1 (n=11)
Flow speed (nm/s)
Flow towards the anterior
No Flow
Flow towards the posterior
E
wild type embryo
ani-1;pig-1 embryo
$T_1$
$T_2$
$T_1$↑
$T_2$
$T_1$↓
$T_2$
$T_1$↓
$T_2$
cortical bleb
cortical bleb
MT pulling
Local flow
Cytoplasmic flow
Furrow shift
Increased anterior cortical myosin level
Decrease of cortical myosin level
Cortical expansion due to cortical blebbing
Pressure decrease due to cortical blebbing

Figure 7

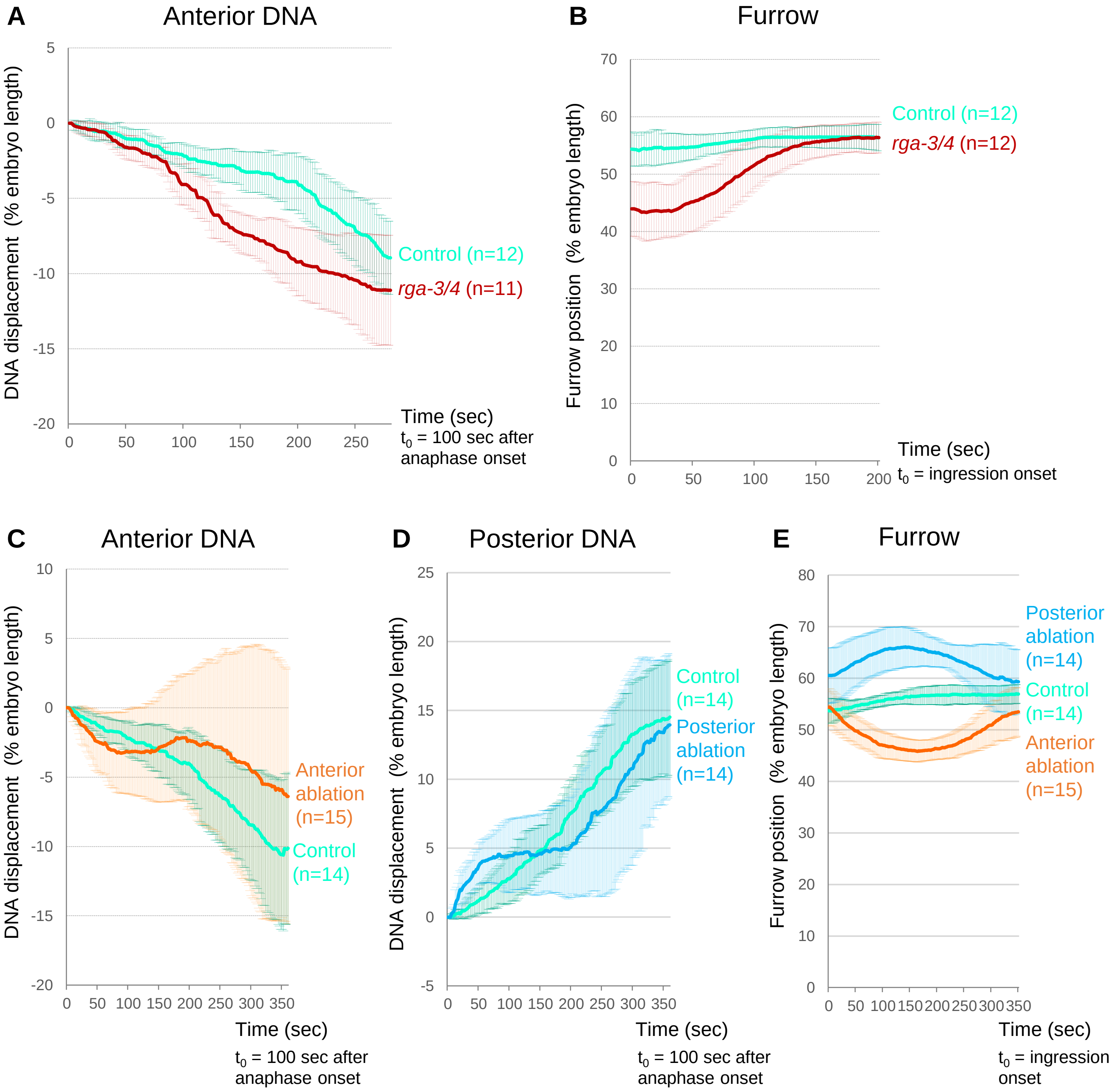

**Figure S1. Correction of DNA segregation defects involves both nuclear and furrow displacement. Related to Figure 2. A.** Average displacement of the anterior nucleus in control and *rga-3/4(RNAi)* embryos. **B.** Average furrow tip position in control and *rga-3/4(RNAi)* embryos. **C-D.** Average displacement of the anterior (C) and posterior (D) nuclei in control embryos and in embryos in which the anterior (C) or posterior (D) centrosome was ablated during early anaphase. **E.** Average furrow tip position in control embryos and in embryos in which the anterior or posterior centrosome was ablated during early anaphase. In A-E, only embryos with corrected DNA segregation defects were analysed.

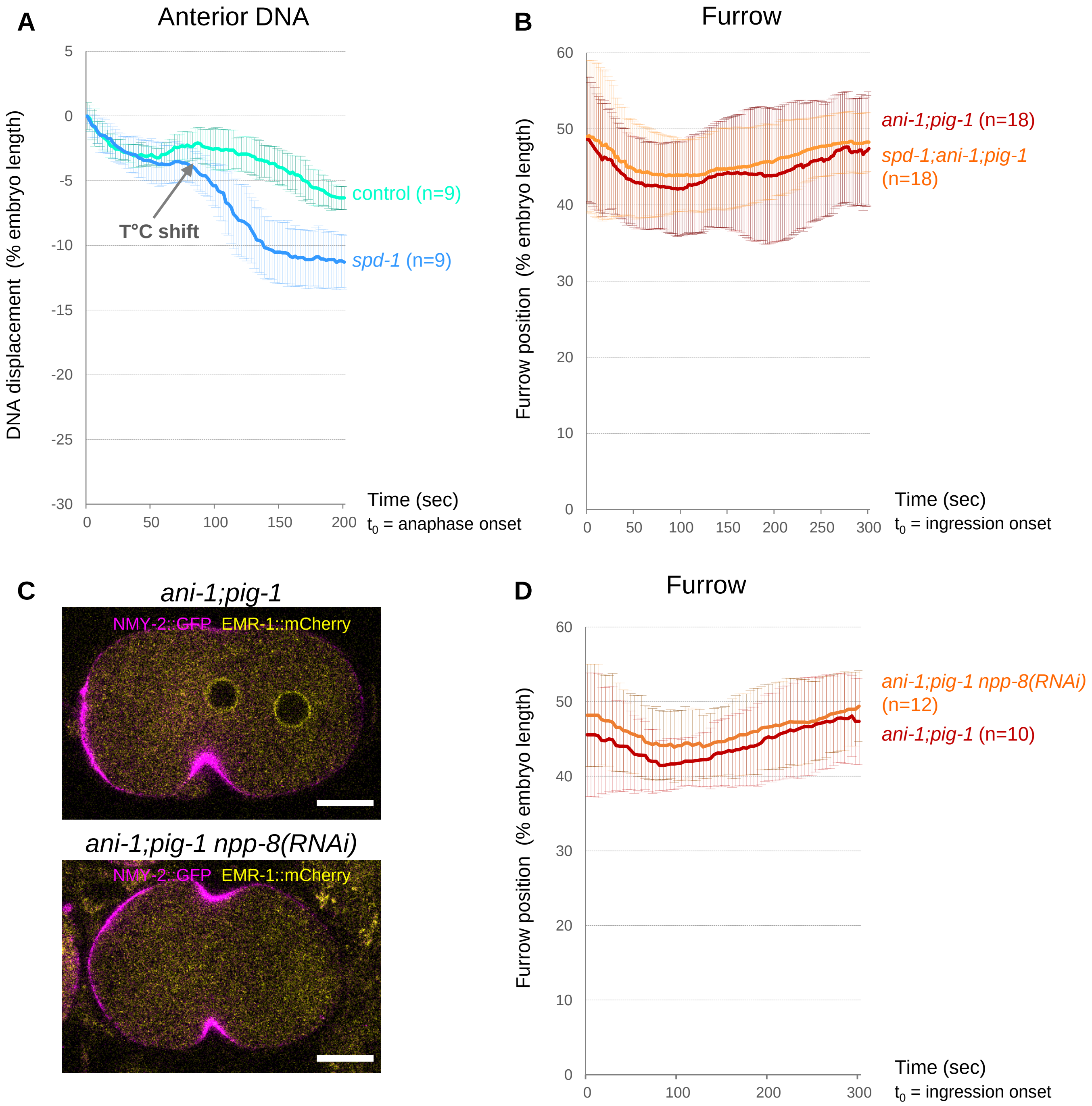

**Figure S2. Central spindle and nuclear envelop formation are not required for furrow displacement. Related to Figure 7. A.** Average displacement of the anterior nucleus in control and *spd-1(oj5)* embryos. In *spd-1(oj5)* embryos, anterior nucleus displacement is accelerated upon temperature shift, indicating efficient central spindle disruption. **B.** Average furrow tip position in *ani-1(RNAi);pig-1(gm344)* and *spd-1(oj5)*;*ani-1(RNAi);pig-1(gm344)* embryos. Only embryos with corrected DNA segregation defects were analysed. All displayed cortical blebbing on the anterior side of the furrow. Rescue efficiency was similar for *ani-1(RNAi);pig-1(gm344)* and *spd-1(oj5)*;*ani-1(RNAi);pig-1(gm344)* embryos (75% and 73% rescue, respectively). **C.** *ani-1(RNAi);pig-1(gm344)* and *ani-1(RNAi);pig-1(gm344) npp-8(RNAi)* embryos expressing NMY-2::GFP (magenta) and EMR-1::mCherry (yellow). No nuclear envelope reformation is observed when *npp-8* is depleted. Scale bar: 10 µm. **D.** Average furrow tip position in *ani-1(RNAi);pig-1(gm344)* and *ani-1(RNAi);pig-1(gm344) npp-8(RNAi)* embryos. Only embryos with corrected DNA segregation defects were analysed. *ani-1(RNAi);pig-1(gm344)* and *ani-1(RNAi);pig-1(gm344) npp-8(RNAi)* embryos present similar frequencies of cortical blebbing on the anterior side of the furrow (90% and 83% of rescued embryos, respectively) and similar rescue efficiency (91% and 100% rescue, respectively). See also video S10.

| Figure | Strains used | RNAi | Incubation Conditions | Recording Temperature |
|---|---|---|---|---|
| Figure 1A<br>Video S1-2 | FL160<br>FL188 | 1 mM IPTG,<br>L4440/ani-1 | 20°C, 30-40h | 23°C (Cherry Temp) |
| Figure 1B<br>Video S3 | FL201<br>FL202 | 1 mM IPTG,<br>L4440/ani-1 | 20°C, 30-40h | 23°C (Cherry Temp) |
| Video S4 | FL212<br>FL216 | 1 mM IPTG,<br>L4440/ani-1 | 15°C, 15-20h | 15°C, shift at 24°C at anaphase onset (Cherry Temp) |
| Figure 1C<br>Video S5 | ANA071<br>FL256 | 1 mM IPTG,<br>L4440/ani-1 | 20°C, 30-40h | 23°C (Cherry Temp) |
| Figure 1D<br>Video S6 | FL160 | 3 mM IPTG,<br>L4440/rga-3/4 | 25°C, 48h | 23°C (Cherry Temp) |
| Figure 1E-F<br>Video S7 | FL235 | OP50 | 20°C, 24h | 20°C (Cherry Temp) |
| Figure 2A-D | FL160<br>FL188 | 1 mM IPTG,<br>L4440/ani-1 | 20°C, 30-40h | 23°C (Cherry Temp) |
| Figure 3A | FL212<br>FL216<br>FL217<br>FL218 | 1 mM IPTG,<br>L4440/ani-1 | 15°C, 15-20h | 15°C, shift at 24°C at anaphase onset (Cherry Temp) |
| Figure 3B | FL160<br>FL207 | 1 mM IPTG,<br>L4440 | 15°C, 15-20h | 15°C, shift at 24°C at anaphase onset (Cherry Temp) |
| Figure 3C | FL188<br>FL208 | 1 mM IPTG,<br>ani-1 | 15°C, 15-20h | 15°C, shift at 24°C at anaphase onset (Cherry Temp) |
| Figure 4A | OD56<br>FL221 | 1 mM IPTG,<br>L4440 | 15°C, 20-25h | 18°C, shift at 25.5°C 220 sec after anaphase onset (Cherry Temp) |
| Figure 4B | FL214<br>FL213 | 1 mM IPTG,<br>ani-1 | 15°C, 20-25h | 18°C, shift at 25.5°C 220 sec after anaphase onset (Cherry Temp) |
| Figure 4C | OD56<br>FL221<br>FL226<br>FL232 | 1 mM IPTG,<br>L4440 | 15°C, 20-25h | 18°C, shift at 25.5°C 220 sec after anaphase onset (Cherry Temp) |
| Figure 4D | FL214<br>FL213<br>FL229<br>FL230 | 1 mM IPTG,<br>ani-1 | 15°C, 20-25h | 18°C, shift at 25.5°C 220 sec after anaphase onset (Cherry Temp) |
| Figure 4E-F<br>Video S8 | FL220<br>FL233 | 1 mM IPTG,<br>ani-1 | 15°C, 20-25h | 18°C, shift at 25.5°C 220 sec after anaphase onset (Cherry Temp) |
| Figure 5A | FL160<br>FL188 | 1 mM IPTG,<br>L4440/ani-1 | 20°C, 30-40h | 23°C (Cherry Temp) |
| Figure 5B-C<br>Video S9 | FL160<br>FL188 | 1 mM IPTG,<br>L4440/ani-1 | 20°C, 20-25h | Room temperature (~19-21°C) |
| Figure 6A,C-D | FL188 | 1 mM IPTG,<br>ani-1 | 20°C, 30-40h | 23°C (Cherry Temp) |
| Figure 7A-B<br>Video S11 | FL188 | 1 mM IPTG,<br>ani-1 | 20°C, 30-40h | 23°C (Cherry Temp) |
| Figure 7C,<br>Video S12 | FL227<br>FL228 | 1 mM IPTG,<br>L4440/ani-1 | 20°C, 30-40h | 23°C (Cherry Temp) |
| Figure 7D | FL227<br>FL225 | 1 mM IPTG,<br>ani-1 | 15°C, 20-25h | 18°C, shift at 25°C at anaphase onset (Cherry Temp) |
| Figure S1A-B | FL160 | 3 mM IPTG,<br>L4440/rga-3/4 | 25°C, 48h | 23°C (Cherry Temp) |
| Figure S1C-E | FL235 | OP50 | 20°C, 24h | 20°C (Cherry Temp) |
| Figure S2A | FL160<br>FL209 | OP50 | 15°C, 24h | 15°C, shift at 25°C 60 sec after anaphase onset (Cherry Temp) |
| Figure S2B<br>Video S10A | FL188<br>FL223 | 1 mM IPTG,<br>ani-1 | 15°C, 15-20h | 15°C, shift at 25°C 60 sec after anaphase onset (Cherry Temp) |
| Figure S2C | FL202 | 1 mM IPTG,<br>ani-1+L4440/<br>ani-1+npp-8 | 20°C, 30-40h | 23°C (Cherry Temp) |
| Figure S2D<br>Video S10B | FL188 | 1 mM IPTG,<br>ani-1+L4440/<br>ani-1+npp-8 | 20°C, 30-40h | 23°C (Cherry Temp) |

**Table S1. RNAi and temperature conditions used for each experiment. Related to STAR Methods**